Monthly Notices of the ROYAL ASTRONOMICAL SOCIETY

MNRAS **543,** 2534–2552 (2025) https://doi.org/10.1093/mnras/staf1577
Advance Access publication 2025 September 17

Modelling the emission lines from r-process elements in supernova nebulae

Giacomo Ricigliano [1]★ Kenta Hotokezaka[2] and Almudena Arcones [1,3,4]

[1]*Institut für Kernphysik, Technische Universität Darmstadt, Schlossgartenstr. 2, Darmstadt D-64289, Germany*
[2]*Research Center for the Early Universe, University of Tokyo, Hongo 7-3-1, Bunkyo, Tokyo 113-0033, Japan*
[3]*GSI Helmholtzzentrum für Schwerionenforschung GmbH, Planckstr. 1, Darmstadt D-64291, Germany*
[4]*Max-Planck-Institut für Kernphysik, Saupfercheckweg 1, Heidelberg D-69117, Germany*

Accepted 2025 September 12. Received 2025 July 25; in original form 2025 February 22

ABSTRACT

The origin of heavy r-process elements in the Universe is still a matter of great debate, with a confirmed scenario being neutron star (NS) mergers. Additional relevant sites could be specific classes of events, such as gamma-ray burst (GRB) supernova, short-plural form = SNe, long-plural form = supernovae (SNs), where a central engine could push neutron-rich material outwards, contributing to the ejecta of the massive exploding star. Here, we investigate our ability to infer the production of heavy elements in such scenarios, on the basis of the observed nebular emission. We solve the steady-state ionization, level population, and thermal balance, for optically thin ejecta in non-local thermodynamic equilibrium (NLTE), in order to explore the role of heavy elements in cooling the gas, and their imprint in the emergent spectrum a few hundreds days post-explosion. We find that heavy elements would be relevant in the cooling process of the nebula only if they account for at least ~ 1 per cent of the total ejected mass, at the typical kinetic temperatures of a few thousands K. However, even in the absence of such amount, a few 0.1 per cent of the total ejected mass could be instead sufficient to leave a detectable imprint around ~ 1–10 μm. This wavelength range, which would be relatively clean from features due to light elements, would be instead robustly populated by lines from heavy elements arising from forbidden transitions in their atomic fine structures. Hence, the new generation of telescopes, represented by the *James Webb Space Telescope* (*JWST*), will most likely allow for their detection.

Key words: stars: neutron – transients: supernovae.

1 INTRODUCTION

The search for astrophysical sites capable of harboring r-process nucleosynthesis has been ongoing for more than half a century (Burbidge et al. 1957; Cameron 1957; Horowitz et al. 2019; Cowan et al. 2021; Perego, Thielemann & Cescutti 2021). Only recently, the detection of the gravitational wave (GW) signal GW170817 (Abbott et al. 2017a), in coincidence with the optical to infrared (IR) electromagnetic (EM) counterpart AT 2017gfo (Abbott et al. 2017b), confirmed that binary neutron star (BNS) mergers eject to some extent neutron-rich material undergoing r-process (Lattimer & Schramm 1974; Eichler et al. 1989; Freiburghaus, Rosswog & Thielemann 1999), the radioactivity of which powers the transient known as kilonova, short-plural form = KNe, long-plural-form = kilonovae (KN) (Li & Paczynski 1998; Metzger et al. 2010; Barnes & Kasen 2013; Tanaka & Hotokezaka 2013; Metzger 2020). Observations of radioactive isotopes on Earth (Wallner et al. 2015; Hotokezaka, Piran & Paul 2015), as well as metal-poor stars in the Milky Way Halo and in dwarf galaxies such as Reticulum II (Ji et al. 2016; Macias & Ramirez-Ruiz 2018; Kirby et al. 2020), require the candidate r-process scenario to be rare and high-yielding. While these conditions can in principle be satisfied by BNS mergers (see e.g. Hotokezaka, Beniamini & Piran 2018), other types of events could still result in similar production rates. Therefore, whether BNS mergers account for the entirety of the observed r-process elements or not remains a matter of debate (Hotokezaka et al. 2018; Côté et al. 2019; Molero et al. 2020; Kobayashi et al. 2023; Beniamini & Piran 2024; Maoz & Nakar 2025).

Other candidates, for which still no evidence for r-process ignition has been firmly obtained, include special classes of core-collapse (CC) SNs, such as magnetorotational (MR) SNs, where the resulting proto-neutron star (PNS) has a high degree of rotation and magnetization (Symbalisty, Schramm & Wilson 1985; Nishimura et al. 2006; Winteler et al. 2012; Barnes et al. 2018; Mösta et al. 2018; Shankar et al. 2021; Reichert et al. 2023). Another example are collapsars, in which the collapsing massive star core produces a black hole (BH)-disc system similar to the NS merger case (MacFadyen & Woosley 1999; Pruet, Woosley & Hoffman 2003; Kohri, Narayan & Piran 2005; Surman, McLaughlin & Hix 2006; Siegel, Barnes & Metzger 2019; Siegel et al. 2022). In particular, despite the higher rarity of collapsars with respect to BNS mergers, Siegel et al. (2019) argued that the large amount of ejecta from these events could be the explanation for most of the r-process elements observed in the Universe (but see also Miller et al. 2020; Just et al. 2022; Fujibayashi et al. 2023; Dean & Fernández 2024, for the viability of r-process nucleosynthesis in collapsar simulations). Notably, the remarkable mass of ^{56}Ni produced (about a few 0.1 $M_\odot$), coupled with the powerful central engine activity, results in significantly brighter SNs, when compared to normal CC SNs. The presence of heavy

★ E-mail: giacomo.ricigliano@gmail.com

elements would then cause a reddening of the SN light curve, but only assuming a good enough mixing of the r-process material in the ejecta (Barnes & Metzger 2022; Barnes & Duffell 2023). High accretion rates onto the central BH, or the interaction between the PNS magnetic field and its surrounding envelopes, can support the launch of relativistic jets giving rise to a long GRB (Woosley 1993; Wheeler et al. 2000; Bucciantini et al. 2008; Metzger et al. 2011). Intriguingly, the recent detection of the long GRB 211211A (Rastinejad et al. 2022) and GRB 230307A (Levan et al. 2023), in association to a KN-like emission, has reignited the question on the progenitor of such events, while providing new examples for a link between GRBs and r-process nucleosynthesis.

SN emissions observed in coincidence of a long GRB have been characterized by very broad spectral lines at early times, corresponding to ejecta velocities up to $\sim 0.1\ c$ (see e.g. Modjaz et al. 2016). The general absence of optical He I lines, in addition to H lines, classifies such events as broad-line (BL) Type Ic SNe. This indicates that the progenitor must have lost the H and most of the He envelope at some point during its evolution [stripped-envelope (SE) SN], falling under the Wolf–Rayet (WR) class of stars (Georgy et al. 2009; Dessart et al. 2011; Liu et al. 2016). In this regard, the long GRB 980425/SN 1998bw represents a famous example of detection displaying the above features (Galama et al. 1998; Iwamoto et al. 1998; Woosley, Eastman & Schmidt 1999). With an estimated ^{56}Ni yield between ~ 0.1–$0.5\ \mathrm{M}_\odot$, this event was likely attributed to the aspherical explosion of a rapidly rotating massive WR star evolving at low metallicity (Dessart et al. 2017). While so far there have been several tens of GRB/SN associations, only SN 1998bw and other two successive events, i.e. GRB 060218/SN 2006aj (Mazzali et al. 2006) and GRB 171205A/SN 2017iuk (Wang et al. 2018), where found at a distance closer than ~ 200 Mpc, allowing for a more detailed study of the emission components. Initially, analysis have been mainly focused on the optical wavelengths, both at early and late times, more than the IR range, mostly due to the lower signal-to-noise ratio (SNR) in that region. However, the progressive upgrades in the capabilities of observatories such as the Very Large Telescope (VLT), and the launch of new space telescopes, like *Spitzer* or, now, the *James Webb Space Telescope* (*JWST*), has opened the possibility for a much more sensitive and deeper search (see e.g. Stritzinger et al. 2024; Cartier et al. 2024).

In this context, while optical/IR photometry of known SE SNe has been targeted at finding signatures of r-process production (Anand et al. 2024), to date there have not been investigations on the possibility of identifying r-process elements in the spectra of such transients. The first days of emission, corresponding to the photospheric phase of the ejecta, are generally characterized by an absorption spectrum poor in recognizable features, due to the high velocities blending the dense line population. As time evolves and the ejecta enters the nebular phase, the spectrum morphs to be dominated by emission features. In particular, heavy elements would be expected to contribute with lines in the IR region, due to the lower opacity associated to the forbidden transitions between levels in their complex f-shell structures. Following GW170817, renovated efforts have been spent in modelling accurately the nebular emission resulting from the NS merger ejecta after ~ 1 week of expansion (Hotokezaka et al. 2021, 2022; Pognan, Jerkstrand & Grumer 2022a; Pognan, Jerkstrand & Grumer 2022b; Hotokezaka et al. 2023; Pognan et al. 2023, 2024; Banerjee et al. 2025). Such works resulted in the discovery of possible candidates in Se or W (Hotokezaka et al. 2022), Te (Hotokezaka et al. 2023), and Rb (Pognan et al. 2023), in addition to those inferred from the photospheric phase, i.e. Sr or He (Watson et al. 2019; Domoto et al. 2021; Gillanders et al. 2022; Perego et al. 2022; Tarumi et al. 2023; Sneppen et al. 2024b, a), Y (Sneppen & Watson 2023), and La and Ce (Domoto et al. 2022). Nebular models have to take into account that the outflow is in NLTE. As such, they require the treatment of both radiative and collisional processes relevant in determining the atomic ionization and level population, from which the emission spectrum is derived.

In this work, we adopt and expand the nebular emission modeling proposed by Hotokezaka et al. (2021), in order to explore for the first time the possible presence of heavy elements in the ejecta from BL Type Ic SNe. The paper is structured as follows. In Section 2, we describe the model employed, including its assumptions, and the treatment of the relevant atomic processes. The input data required by the latter are listed in Section 3 (integrated by Appendix A), while an exploration of its parameter space is conducted in Section 4. We spend Sections 5 and 6 to note the overall impact that an r-process composition would have in the heating and cooling processes of the ejecta, respectively. Our model is then benchmarked against a characteristic spectrum of a BL Type Ic SN, i.e. SN 1998bw, in Section 7.1. Finally, we investigate possible signatures or r-process elements in such a scenario in Section 7.2, discussing the robustness of our results in Section 7.3. Our main takeaways are thus summarized in Section 8.

2 NEBULA MODELLING

Following Hotokezaka et al. (2021), we model the nebular emission of an expanding ejecta in an explosive event by introducing a series of simplifying conditions. First, we assume that the fluid is in a steady-state regime, i.e. that the atomic processes at the source of the emission are much faster than the fluid expansion. This is reasonably valid at an early enough stage, where the recombination time-scale is much shorter than the dynamical time-scale (Pognan et al. 2022a). This condition holds in our model, where the typical electron number density is $\gtrsim 10^6\ \mathrm{cm}^{-3}$ at $\mathcal{O}(100)$ d after the explosion. Secondly, we consider the ejecta to be optically thin, whereas the final spectrum will be dominated by pure emission. Such an assumption heavily simplifies our photon transport modelling, which is limited to the effective treatment of the local self-absorption. However, we recall that this approach loses validity when different lines contribute in the same wavelength region, as it can be the case for optical emissions from lanthanides.

We describe the ejecta at a fixed epoch using a multizone approach, where each zone is characterized by a density value and an elemental composition. In order to determine the ion abundances within a zone, we solve the steady-state ionization balance:

$$\frac{\mathrm{d}n_i^p}{\mathrm{d}t} = -\gamma_{i,\mathrm{tot}}^p n_i^p + \alpha_{i+1}^p n_{i+1}^p n_\mathrm{e} \approx 0\,, \tag{1}$$

where n_i^p indicates the number density of an element p in ionization stage i (hereafter species $\{p, i\}$), such that $\sum_{p,i} n_i^p = n$ and $\sum_{p,i} i n_i^p = n_\mathrm{e}$, with n and n_e the atoms and free electrons number density, respectively. Here, α_{i+1}^p is the total recombination rate coefficient for the species $\{p, i+1\}$ to recombine into $\{p, i\}$, obtained in general by summing the contributions from both radiative and dielectronic recombination processes. Concurrently,

$$\gamma_{i,\mathrm{tot}}^p = \gamma_{i,\mathrm{rad}}^p + \gamma_{i,\mathrm{rec}}^p \tag{2}$$

is the total ionization rate per atom for the species $\{p, i\}$ to ionize into $\{p, i+1\}$. Equation (2) shows the relevant contributions to ionization.

At the times of the nebular phase, we assume that the main source of ionization is represented by the radioactivity of the ejected material. Radioactive energy is mainly released via β-particles produced in β-decays and γ-rays produced in nuclear de-excitations, with the second channel typically prone to leak out of the ejecta due to the low medium opacity, leaving the first channel responsible for the energy deposition. The heating rate as a function of time depends on which decaying species dominate the ejecta composition, ranging from a simple exponential chain, as in a Ni-powered SN, to a power law, as in the case of an r-process-powered KN. However, the energy deposition rate soon deviates from the instantaneous radioactive energy generation, as the thermalization of β-particles becomes inefficient. For arbitrary r-process compositions, we treat radioactivity and thermalization using the model described in Hotokezaka & Nakar (2020). Given a thermalized heating rate per unit volume Γ, the ionization rate per atom due to radioactivity is then

$$\gamma^p_{i,\mathrm{rad}} = \frac{\Gamma}{w^p_i n^p_i}\,, \tag{3}$$

where w^p_i is the work per ion pair, i.e. the energy dissipated by a produced β-particle in causing one $\{p,i\}$ ionization event in the stopping plasma. Here, we describe the work per ion pair as $w^p_i = wI^p_i$, with I^p_i the species $\{p,i\}$ first ionization potential, and w a model parameter. Informed by the estimates of Hotokezaka et al. (2021), we fix the value of w to 15 throughout this work.

Secondly, we include in our model the contribution to ionization due to recombination photons, for which the ejecta is optically thick in the nebular phase. This effect can be particularly important at low densities, where lightly ionized species are favoured. We define the probability for a photon created in the recombination event of species $\{q,j\}$ to ionize species $\{p,i\}$ as

$$P^{pq}_{ij} = \int (1-e^{-\tau})\frac{n^p_i\sigma^p_i}{\sum_{r,k} n^r_k\sigma^r_k}\left(\frac{\mathrm{d}N_{\mathrm{ph}}}{\mathrm{d}\nu}\right)^q_j \mathrm{d}\nu\,, \tag{4}$$

where σ^p_i is the photoionization cross-section of species $\{p,i\}$, $\left(\frac{\mathrm{d}N_{\mathrm{ph}}}{\mathrm{d}\nu}\right)^q_j$ is the spectrum of photons emerging from the recombination of species $\{q,j\}$, and τ is the photon optical depth, which we define as

$$\tau = R\sum_{r,k} n^r_k\sigma^r_k\,, \tag{5}$$

with R the dimension of the zone. While photons emerging from radiative recombinations have roughly energies close to the first ionization potential of the recombining species, the photons cascade of dielectronic processes has a generally unknown spectrum. Here, we assume that photons are emitted in similar number at all energy scales between the first ionization potential of the recombining species and the first ionization potential of its neutral counterpart, i.e.

$$\left(\frac{\mathrm{d}N_{\mathrm{ph}}}{\mathrm{d}\nu}\right)^q_j = \frac{1}{1-\frac{I^q_0}{I^q_j+k_{\mathrm{B}}T_{\mathrm{e}}}}\frac{1}{\nu} \quad \text{with} \quad I^q_0 < \nu < I^q_j + k_{\mathrm{B}}T_{\mathrm{e}}\,, \tag{6}$$

where we also account for a thermal energy budget. The ionization rate per atom due to recombination photons is then

$$\gamma^p_{i,\mathrm{rec}} = \sum_{q,j:I^q_j+k_{\mathrm{B}}T_{\mathrm{e}}\geq I^p_i} P^{pq}_{ij}\alpha^q_{j+1}n^q_{j+1}n_{\mathrm{e}} + \\ + \sum_{q,j:I^q_j+k_{\mathrm{B}}\bar{T}_{\mathrm{e}}\geq I^p_i} \bar{P}^{pq}_{ij}\bar{\alpha}^q_{j+1}\bar{n}^q_{j+1}\bar{n}_{\mathrm{e}}e^{-\bar{\tau}}\,, \tag{7}$$

where the sum includes all recombining species able to produce photons energetic enough to ionize species $\{p,i\}$. In equation (7), we account for the contributions to ionization from recombination events taking place in the adjacent inner zone, indicated by the barred version of each quantity. Such contributions are weighted with a diffusion factor depending on the optical depth of the inner zone.

The level population of each ion species is found by solving the steady-state level balance:

$$\frac{\mathrm{d}n_m}{\mathrm{d}t} = \sum_{l:l\neq m}(n_l n_{\mathrm{e}}k_{lm} - n_m n_{\mathrm{e}}k_{ml}) + \\ - \sum_{l:l<m}\langle\beta_{ml}\rangle n_m A_{ml} + \sum_{l:l>m}\langle\beta_{lm}\rangle n_l A_{lm} \approx 0\,, \tag{8}$$

with n_m the number density of an ion species $\{p,i\}$ in a level m, such that $\sum_m n_m = n^p_i$. Note that we dropped both the p and i indices for convenience, since the level equations for different species are completely decoupled, as a consequence of assuming the ejecta to be optically thin (apart from self-absorption). Equation (8) accounts for all electron collisional transitions between a level m and any other level l, described by the collisional rate coefficient k_{ml}, as well as for all radiative transitions from a level m to a lower level l, described by the radiative transition rate per atom A_{ml}, and characterized by a transition frequency ν_{ml}. We treat photon self-absorption by applying an escape probability $\langle\beta_{ml}\rangle$ to the radiative transition between state m and l, which we define as

$$\langle\beta_{ml}\rangle = \frac{1-e^{-\tau_{ml}}}{\tau_{ml}}\,, \tag{9}$$

where τ_{ml} is the Sobolev optical depth for that transition. For the collisional transitions, the collisional rate coefficient for de-excitations takes the form

$$k_{lm} = \frac{8.63\times10^{-6}\Omega_{lm}(T_{\mathrm{e}})}{g_l T^{\frac{1}{2}}_{\mathrm{e},1}}\ \mathrm{cm^3\ s^{-1}}\,, \tag{10}$$

with $l>m$, g_l the level l degeneracy, Ω_{lm} the correspondent collision strength, and $T_{\mathrm{e},1}$ the kinetic temperature in units of K. Accordingly, the collisional rate coefficient for excitations follows

$$k_{ml} = \frac{g_l}{g_m}k_{lm}e^{-\frac{E_{lm}}{k_{\mathrm{B}}T_{\mathrm{e}}}}\,. \tag{11}$$

The contribution to the ejecta cooling rate density Λ from a species $\{p,i\}$ is then computed as the sum over all the associated radiative de-excitations:

$$\Lambda = \sum_{m,l:m>l} n_m E_{ml}\langle\beta_{ml}\rangle A_{ml}\,, \tag{12}$$

where E_{ml} is the energy gap between level m and l. The ion and level populations are thus solved iteratively for different values of the kinetic temperature T_{e}, until thermal balance is satisfied, i.e.

$$\Gamma - \sum_{p,i}\Lambda^p_i \approx 0\,, \tag{13}$$

where we reintroduced the indices p and i in order to indicate the different ions.

From the above ejecta snapshot, we derive an emission spectrum by summing over all the lines of every ion. The contribution to the luminosity from a single ion species $\{p,i\}$ is then

$$L_\nu = \sum_{m,l:m>l} N_m E_{ml}\langle\beta_{ml}\rangle A_{ml}\mathcal{N}_\nu\left(\nu_{ml}, \left(\frac{\nu_{ml}v}{\sqrt{2}c}\right)^2\right)\,, \tag{14}$$

where N_m is the number of atoms in level m, while $\mathcal{N}_v$ is the normal distribution, which we use to characterize the line spread due to the zone velocity v shift. Note that in the last equation we dropped again the p and i indices for simplicity. We reintroduce them right after, as, finally, the total luminosity is thus

$$L_v = \sum_{p,i} L^p_{i,v} \,. \tag{15}$$

3 ATOMIC DATA

We report here the data used to solve the ionization balance of the ions and model the nebular emission from r-process elements. The remaining set of atomic data for lighter elements, necessary to calculate the level population and the emergent spectrum, including energy levels, radiative transition rates, and collision strengths, is listed in Appendix A.

3.1 Line list and radiative transition rates for r-process elements

In order to model heavy elements ($Z \geq 29$), we use the line list provided by Hotokezaka et al. (2022). This list includes magnetic dipole (M1) lines of heavy elements with experimentally calibrated energy levels from the National Institute of Standards and Technology (NIST) Atomic Spectra Database (ASD; Kramida et al. 2021). The radiative M1 transitions from the NIST data base are integrated with the transitions computed using the analytic formula based on LS coupling (Pasternack 1940; Shortley 1940; Bahcall & Wolf 1968) reported in Appendix A (equation A1). For the electric dipole (E1) transitions instead, we exploit the HULLAC calculations carried by Hotokezaka et al. (2021). In particular, we take the Nd E1 cooling power from that work, and we reduce it to characterize all the heavy elements. This choice is motivated by the fact that Nd is among the strongest coolants in the IR, at the nebular temperatures of a few 10^3 K expected. Most of the heavy elements have instead E1 transitions at comparably higher energies, and are therefore not expected to contribute to the same extent at the above temperatures. In order to take into account the variable intensity of such transitions across the periodic table, we thus associate 10 per cent of the original E1 Nd intensity to each element. We address the validity of this approximation in Section 6. However, we do not include such E1 transitions individually when deriving the spectrum (see Section 7.2).

3.2 Collision strengths for r-process elements and general uncertainty in collisional data

For the collision strength of transitions between levels of the ground terms in elements with $Z \geq 29$, we mostly use the data computed by Hotokezaka et al. (2022) with HULLAC. To treat the collision strengths of the remaining lines, we use the approximate formula from van Regemorter (1962) for E1 transitions, by assuming that radiative transition rates are approximately $A \approx 2 \times 10^6 \lambda^{-3}$ s^{-1}, with λ the corresponding wavelength in μm. Instead, following Hotokezaka et al. (2021), we choose a constant value $\Omega_{\rm F} = 1$ for the collision strength of forbidden transitions. Additionally, for the fine structure transitions of the ground term of Te III, we use the data from Madonna et al. (2018). We note that recently new, more accurate atomic data targeted on elements relevant for KNs have been published, including collisional strengths for Sr and Y (Mulholland et al. 2024a), and for Te (Mulholland et al. 2024b). We plan on employing such data in future works, in order to refine our predictions on the detectability of heavy elements.

The collision strengths of relatively important transitions in both light and heavy elements are either the result of HULLAC calculations or those from R-matrix calculations available in the literature (see Appendix A). While the R-matrix method is generally more accurate, for fine structure lines of heavy elements most of the data are those obtained with HULLAC. As discussed in Hotokezaka et al. (2022), the collision strengths from HULLAC often differ from those calculated with the R-matrix method by a factor of 2–5. In addition, the HULLAC values are systematically lower for some ions. These discrepancies suggest that our line intensities can be under- or overestimated by a factor of a few. Furthermore, due to the smaller HULLAC collision strengths, the inferred electron temperature may be overestimated if heavy elements dominate the cooling rate (see Section 6 for a discussion on when this would be the case).

3.3 Recombination rates

We import radiative and dielectronic recombination rates from the available literature and public data bases, and we integrate them with our previously computed data. We include ions up to the fourth ionization stage, as we expect a mild level of ionization at the kinetic temperatures considered $\mathcal{O}(10^3$ K). For the recombination of Fe I-III, and Ni II, we use the values computed using the R-matrix method in an ab initio framework by Nahar (1996, 1997), Nahar, Bautista & Pradhan (1997) and Nahar & Bautista (2001), respectively. Because of the absence of data consistent with the works above, for Ni I, Ni III, and Co ions we assume the values of the respective Fe ionization stages. For lighter elements, we use the analytic fits for both radiative and dielectronic recombination rates provided by Badnell (2006), Bleda, Altun & Badnell (2022), and references therein. Such fits are based on autoionization transition rates computed using the Breit–Pauli Hamiltonian with the AUTOSTRUCTURE codes suite (Badnell 1986), and cover ions up to the P plus Ar isoelectronic sequences. Therefore, in order to fill in the missing data, we integrate the above rates with those provided by the CHIANTI atomic data base (Dere et al. 1997; Zanna et al. 2021), with the caveat that at low electron temperatures $\lesssim \mathcal{O}(10^2$ K), the dielectronic contribution to the total recombination rate is not always available. Finally, for elements heavier than Ni, we assume the same dielectronic recombination rates as were obtained by Hotokezaka et al. (2021) for Nd,[1] using the atomic structure code HULLAC (Bar-Shalom, Klapisch & Oreg 2001), and we use the formula provided by Axelrod (1980) for the radiative recombination of Fe ions:

$$\alpha_{\rm RR} = 3 \times 10^{-13} i^2 \left[\left(\frac{T_{\rm e}}{10^4\ {\rm K}} \right)^{-\frac{3}{2}} - \frac{1}{3} \left(\frac{T_{\rm e}}{10^4\ {\rm K}} \right)^{-\frac{1}{2}} \right] \ {\rm cm^3\ s^{-1}} \,, \tag{16}$$

with i the recombined ion charge.

In this regard, we note that current efforts in producing detailed atomic data for KNs have recently resulted in new total recombination rates for light r-process elements, including the first three ionization stages of Se, Rb, Sr, Y, and Zr (Banerjee et al. 2025). The latter demonstrated how accurate rate calculations can substantially change the predictions on the observed nebular spectra. Despite here we do not include such data yet, leaving it to the further development of

[1]The included rates describe Nd recombinations from stage IV to III and III to II. We use the latter also for stage II to I.

our model, we explore the effects of different ionization levels on our predictions in Section 7.3.

3.4 Photoionization cross-sections

We use photoionization cross-sections for Fe ions computed with HULLAC, in order to characterize all non-neutral species (see Appendix B). Here, we use the `nonrel.config` mode, for which fine structure levels are not resolved. Photoionization on neutrals is instead described starting from the photoabsorption calculations stored in the XCOM data base of the NIST (Scofield 1973). Since the latter consider incident photon energies ranging from 1 to 1500 keV, thus covering only the high energy tail of the recombination photons' distribution, we assume a flat cross-section for lower energies, in continuity with the high energy part. Although our treatment of the photoionzation cross-sections is rather approximate, it is sufficient to roughly estimate the contribution of recombination photons to the overall ionization (which we explore in Appendix B).

4 MODEL APPLICABILITY

The absence of a complete data base including all possible allowed and forbidden atomic transitions for every element inherently hinders the computation of a fully accurate spectrum emergent from a heterogeneous composition consisting of both light and heavy elements. However, using the model described in Section 2 together with the data listed in Section 3, we can already obtain useful estimates, assuming the validity of all the assumptions and approximations employed. In order to test our set-up, we define a one-zone model parameter space which should cover the typical conditions found in the nebular phase of expanding ejecta. For a given composition, we identify two main degrees of freedom for our model, i.e. the amount of heating injected in the system per unit time and unit mass $\dot{\epsilon}$, and the number density of atoms n. We then focus on relevant intervals for these quantities, as suggested by the typical evolution of ejecta from different kind of events. For this purpose, we construct plausible trajectories for different SNs and KNs. Despite in this work we are not specifically interested in each one of these events, we take the opportunity to test the performance of our model in all of the above cases. For the ejecta density, we consider a time-dependent homologous expansion law of the form

$$n(t) = n_0 \left(\frac{t}{t_0}\right)^{-3} , \tag{17}$$

where we arbitrarily set an initial time $t_0 = 10^4$ s, and the corresponding initial density is computed as average over a sphere with mass $M_{\rm ej}$ and velocity $v_{\rm ej}$ depending on the case. We thus model a CC SN with a typical ejecta mass and velocity of $M_{\rm ej}^{\rm CCSN} = 0.5\ {\rm M}_\odot$ and $v_{\rm ej}^{\rm CCSN} = 0.01\ c$ respectively, and we compare it to an SN Type Ia with $M_{\rm ej}^{\rm SNIa} = 1.4\ {\rm M}_\odot$ and $v_{\rm ej}^{\rm SNIa} = 0.03\ c$. Additionally, we construct a KN with $M_{\rm ej}^{\rm KN} = 10^{-2}\ {\rm M}_\odot$ and $v_{\rm ej}^{\rm KN} = 0.1\ c$. The heating evolution counterpart is computed from the ^{56}Ni-Co and ^{44}Ti-Sc decay chains energy input in the SN cases, while for the KN we assume the characteristic r-process heating rate from Metzger (2020):

$$\dot{\epsilon}(t) = 2 \times 10^{10} \left(\frac{t}{1\ {\rm d}}\right)^{-1.3} . \tag{18}$$

In the SN cases we consider a ^{56}Ni mass of $M_{^{56}{\rm Ni}}^{\rm CCSN} = 6.9 \times 10^{-2}\ {\rm M}_\odot$ (the value inferred for SN1987A) and $M_{^{56}{\rm Ni}}^{\rm SNIa} = 0.6\ {\rm M}_\odot$, for the CC SN and the SN Type Ia models respectively. From the KN model instead, we differentiate two cases, by assuming an r-process mass of $M_{\rm r}^{\rm KN} = 10^{-3}\ {\rm M}_\odot$ and $M_{\rm r}^{\rm KN} = 10^{-2}\ {\rm M}_\odot$, respectively. We also produce an alternative trajectory, by considering the CC SN model, and by polluting it with an amount of r-process material equal to its amount of ^{56}Ni. Finally, we compute the energy deposition rates by applying the following thermalization prescriptions. In order to account for the thermalization of γ-rays, we employ the analytic formula from Sharon & Kushnir (2020), specifically tailored on core-collapse SNs, but demonstrated to be a good approximation also for Type Ia SNs and KNs (Guttman et al. 2024):

$$f_{\gamma,{\rm th}}(t) = \frac{1}{\left(1 + \frac{t}{t_0}^n\right)^{\frac{2}{n}}} , \tag{19}$$

where $f_{\gamma,{\rm th}}(t)$ is the fraction of γ-ray energy instantaneously deposited in the ejecta, $t_0 \sim 100$ d is the characteristic γ-ray escape time, and $n \sim 3$ is a parameter that controls the transition between optically thick and optically thin regime. In parallel, we resort to the analytic formula derived by Barnes et al. (2016) in order to characterize the energy deposition of β-particles from the decay of the r-process material, where we assume that 20 per cent of the total decay energy is carried by such channel, while 45 per cent by γ-rays and the remaining is lost with neutrinos. The formula is based on an estimate of the characteristic time at which the thermalization of β-particles becomes inefficient, and it is parametrized by the total ejecta mass and average velocity. Despite most of the above masses and velocities being only broadly informed on the literature and still somewhat arbitrary, the resulting trajectories cover well the parameter space region where these various explosive events live.

As visible in Fig. 1, after ~ 100 d the ejecta from various SNs are heated with $\lesssim 10^9$ erg s^{-1} g^{-1}, and within ~ 700 d the heating rate reaches $\sim 10^5$ erg s^{-1} g^{-1}. Simultaneously, at each time, the density is lower by about one order of magnitude for the faster ejecta of the SN Ia, compared to the CC SN case. Such time interval is expected to bracket the conditions necessary for the steady-state nebular phase of SNs, as illustrated by Axelrod (1980). For a typical KN instead, the same range of conditions are reached much earlier in the ejecta evolution, between a few days and ~ 100 d, with a steeper density decrease due to the considerably faster medium. Notably, as further investigated in Section 5, polluting CC SN ejecta with even a considerable amount of r-process material does not relevantly impact the heating before a few years, when the ^{56}Co decay fades to be soon replaced by the ^{44}Sc decay as main energy source. However, already in the steady-state phase, r-process material may still have a role in the ejecta cooling mechanism (see Section 6).

Also shown in Fig. 1 is the kinetic temperature behaviour within the parameter space considered, for different one-zone toy compositions. The calculations are carried on a 10 $\times$10 log-spaced grid, coupling the ionization balance and the thermal balance to obtain both the correspondent ionic composition and temperature. For simplicity, we consider a system composed by pure Fe (left panel), pure Nd (central panel), and a mixture of Fe and Nd present in equal mass. We stress here that such toy compositions are not meant to be a precise proxy for the systems the trajectories of which have been described above. The correct thermodynamic status of such systems can only be obtained by considering a full realistic time-dependent composition, including elements both lighter and heavier than Fe, several of them potentially having a relevant cooling role. We address this point in Section 6. Instead, here we focus on the considered elements (and a first direct combination of them) for illustrative purposes, grasping the typical behaviour around the conditions of astrophysical interest, whereas such behaviour is qualitatively expected also in richer compositions.

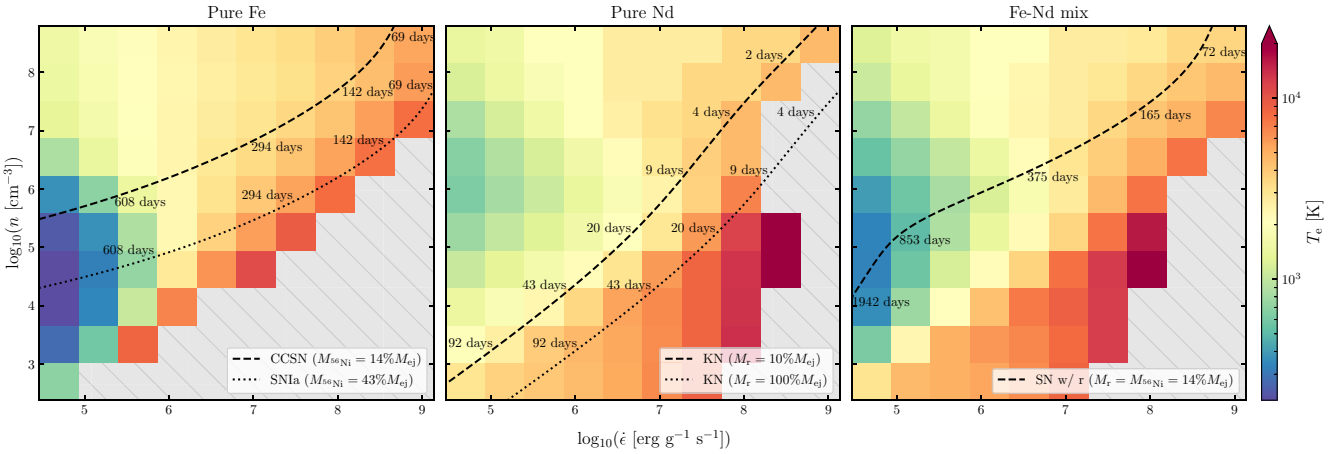

Figure 1. Electron temperature as a function of the specific energy deposition rate and the number density of atoms, for a gas of ions (I–IV) of pure Fe (left panel), pure Nd (central panel), and a mixture of 50 per cent Fe and 50 per cent Nd in mass fraction (right panel). Values are computed on a 10 × 10 grid log-spaced, using ionization and thermal balance. For approximate visual reference, we superimpose plausible trajectories with their time evolution of a CC SN, a SN Ia, a KN with two degrees of r-process material dilution, and a CC SN polluted with r-process material.

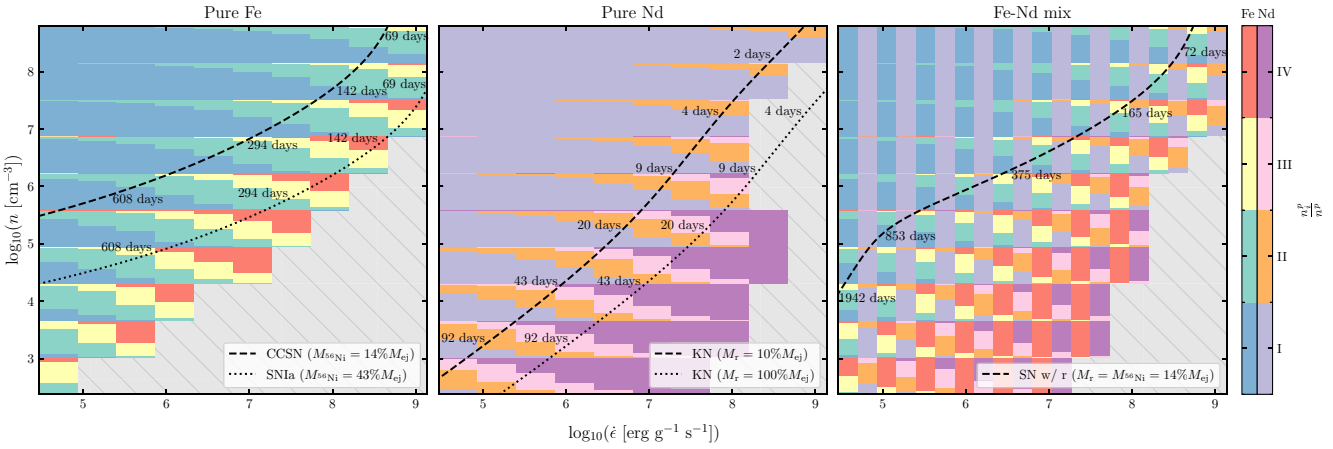

Figure 2. Same as Fig. 1, with the plotted quantity being the number fraction of ions as stacked histogram. For the Fe–Nd mixture case (right panel), the ion fractions of Fe and Nd are displayed on the left and the right side of each grid cell, respectively.

In general, the grid values reflect the cooling ability of the ions, which increases as a function of T_e. Given the imposed thermal balance, as expected T_e always monotonically increases with the input heating, for a fixed density. Roughly all ejecta trajectories lie in a region where the mixture temperature is a few 10^3 K in the steady-state phase, while regions with higher (lower) density and lower (higher) heating are not astrophysically explored. Still, when looking at the different kinds of ejecta, the temperature for Fe shows a stronger excursion, decreasing during the SNs evolution, compared to Nd in KNs. In the latter case, T_e maintains a rather constant value, such that, depending on the ejecta mass and velocity, it can also potentially re-increase, as found by Pognan et al. (2022a) using a much more sophisticated transport model. The result of combining Fe and Nd in very optimistic equal amounts, is the product of a balance between opposing effects. On one side, the amount of each element is trivially reduced, and, with it, its contribution to the overall cooling. On the other side, the presence of different species helps relieving the burden of cooling from a single element, with the most efficient cooler dominating, depending on the specific conditions. In our Fe–Nd case, the main effect of such combination is only a slight redistribution of the kinetic temperature in the grid which contributes to smooth out the sharper landscape of the pure Fe case.

On a different note, Fig. 1 uncovers a model limit, whereas the uncoloured cells correspond to a region where the thermal balance calculation does not converge. This is due to the inability of our model to cool enough in order to compensate for the injected heating, and it is clearly dependent on the considered elemental composition. While it is possible that in this region the system is physically unable to meet the thermal balance constraint within the model framework and assumptions, we note that this limit can also be affected by the specific line list included in the input data (see Section 3), which can substantially change the cooling function of each element.

Completing the picture described above, Fig. 2 shows the number fraction of ion species for each of the toy models considered. In all cases, a lower kinetic temperature of the system leads to a generally lower degree of ionization, with Fe stages I-II favoured over stages III–IV for the instantaneously denser CC SNs, compared to the SN Ia case. Similarly, in the KNs, a lower instantaneous heating due to less r-process material leads to the same effect for Nd ions. This is caused by an increase in the recombination rates for lower temperatures, which are determined by less heating and thus

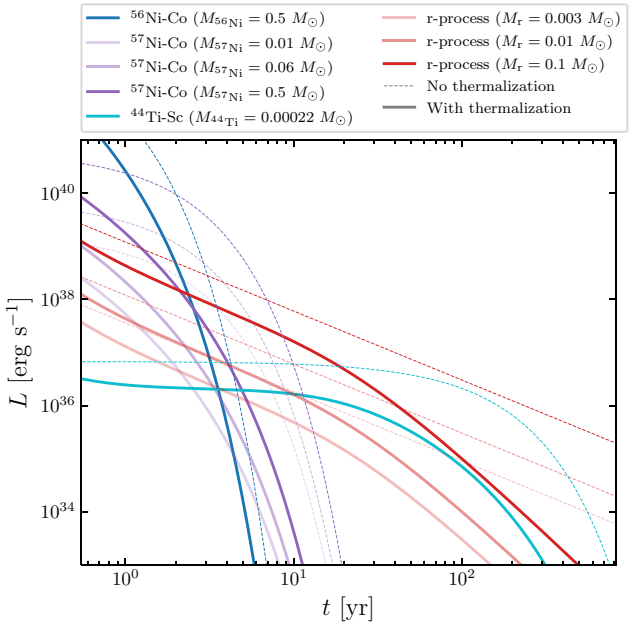

Figure 3. Total radioactive heating from the decay chains of ^{56}Ni–Co and ^{44}Ti–Sc for an SE SN, compared to the decay chain of ^{57}Ni–Co for a variable initial amount of ^{57}Ni, and to the heating due to the decay of a variable amount of r-process material. The values of ^{56}Ni and ^{44}Ti are taken from the CO138H SN model by Nomoto et al. (2000). The radioactive energy produced (dashed lines) is shown for visual reference in contrast to the deposited energy (solid lines).

also lower non-thermal ionization rates. However, this trend is not universal, as evident from the far left region of the parameter space, where, especially for Fe, despite the very low temperatures, the stage II survives. In fact, as listed in Section 2, the computed ionization balance is determined also by the contribution to ionization coming from recombination photons. We asses the impact of such ionization component in Appendix B. Finally, when mixing the two elements, we note that for a fixed kinetic temperature the average ionization stage of Fe is always greater than that of Nd, as a result of the lower recombination rates of Fe ions.

5 HEATING ROLE

In the context of SE SNs, the importance that r-process elements may have in heating the ejecta is directly in competition with the heating from radioactive Ni. Most likely, even an amount of heavy elements relevantly exceeding the typical estimates for BNS mergers would not be sufficient to leave a signature in the SN light curve near peak time, due to the much higher specific energy released by the massive ^{56}Ni content. However, while the time-scales considered in such case correspond to the photospheric phase of the emission, in principle the evolving astrophysical conditions and nuclei involved could lead to a different outcome during the nebular phase.

Fig. 3 shows a simple estimate of the total amount of instantaneous heating coming from the decay chain of ^{56}Ni–Co and ^{44}Ti–Sc, compared to the heating from typical r-process material in variable amount, in the case of an SE SN. We also explore the presence of a significant initial amount of ^{57}Ni, the decay of which could also manifest in the light curve. We consider the mass of ^{56}Ni produced in the explosion to be $M_{^{56}\mathrm{Ni}} = 0.5$ M$_\odot$, and that of ^{44}Ti to be $M_{^{44}\mathrm{Ti}} = 2.2 \times 10^{-4}$ M$_\odot$, as obtained by Nomoto et al. (2000) in their CO138H SN explosion model. Such value of the ^{56}Ni mass roughly represents a conservative upper bound, as inferred from the light curves of SE SNs analysed by Rodríguez, Nakar & Maoz (2024). From the same CO138H model, we also take into account the amount of ^{57}Ni, i.e. $M_{^{57}\mathrm{Ni}} = 1.5 \times 10^{-2}$ M$_\odot$, as a basis from which exploring its relevance. For the thermalization of the decay energy, we use the prescriptions introduced in Section 4, assuming a total ejecta mass of 10 M$_\odot$ and average velocity 0.02 c (see, e.g. Nakamura et al. 2001).

As shown in Fig. 3, a few times 10^{-3} M$_\odot$ of r-process material would be sufficient to eventually emerge in the light curve, in a limited time interval. A mass of r-elements of a few times 10^{-2} M$_\odot$ would then dominate the emission for several years between the ^{56}Co and the ^{44}Sc contributions, potentially being comparable to the decay of ^{44}Sc around present time. Higher amounts would completely eclipse the ^{44}Ti decay chain source, dominating the overall energy release and lead the emission already from a few years post-explosion on, once the ^{56}Co decay has past its activity peak.

On the other hand, the presence of r-process elements could be partially hidden also by the heating from the ^{57}Ni decay chain. While the CO138H model from Nomoto et al. (2000) predicts a mass of ^{57}Ni which is too low to be visible, starting from a relative amount of ^{57}Ni/^{56}Ni ~ 0.12, the imprint of ^{57}Co decay would be relevant in the same time window as the r-process heating. However, because of the steeper decrease in the decay heating, even a very optimistic content of ^{57}Ni matching the one of its lighter isotope (^{57}Ni/^{56}Ni ~ 1) would leave room for $\sim 10^{-2}$ M$_\odot$ of r-process material to be seen.

Notably, these alternative sources of energy would reveal themselves in the observed luminosity, due to the different slope, and assuming no additional source as a central engine. In the case of SN 1998bw, however, the time interval of interest is currently left unexplored, since the most recent work reconstructing a quasi-bolometric luminosity from available photometric data includes observations only up to ~ 500 d post-GRB (Clocchiatti et al. 2011).

6 COOLING ROLE

Independently from the role played in heating up the ejecta, a sufficient amount of heavy elements could add a relevant contribution to the cooling of the system already in the steady-state nebular phase, when the ^{56}Co decay is supposed to be the main source of energy. We investigate the r-process material cooling power, by considering sets of different toy mixtures, constructed as follows:

(i) for elements with $Z \leq 30$, we use alternatively the abundance pattern of the S25 SN model from Rauscher et al. (2002), based on a 25 M$_\odot$ zero-age main sequence (ZAMS) progenitor, or the r0e2 model from Dessart et al. (2017), based on a 40 M$_\odot$ ZAMS progenitor (see also Section 7);
(ii) for elements with $Z > 30$, we use the solar r-process component pattern as derived by Prantzos et al. (2020).

We thus group the elements into light ($Z \leq 30$) and heavy ($Z > 30$) ones, and we extract from the first group a third one constituted by the iron group elements with $Z = 26, 27, 28$. Their total mass fractions, i.e. X_lights, X_heavies, and X_iron, respectively, are then varied in order to create the different sets of abundances. We start by considering two compositions without heavy elements, representing considerably different base scenarios, with a higher relative production of iron coupled with the S25 model, and a lower relative production of iron combined with the r0e2 model. These cases are generally inspired by a CC SN such as SN 1987A, and by an SE SN such as SN 1998bw, respectively. We note here that the mass fraction of iron does not reflect in general the absolute

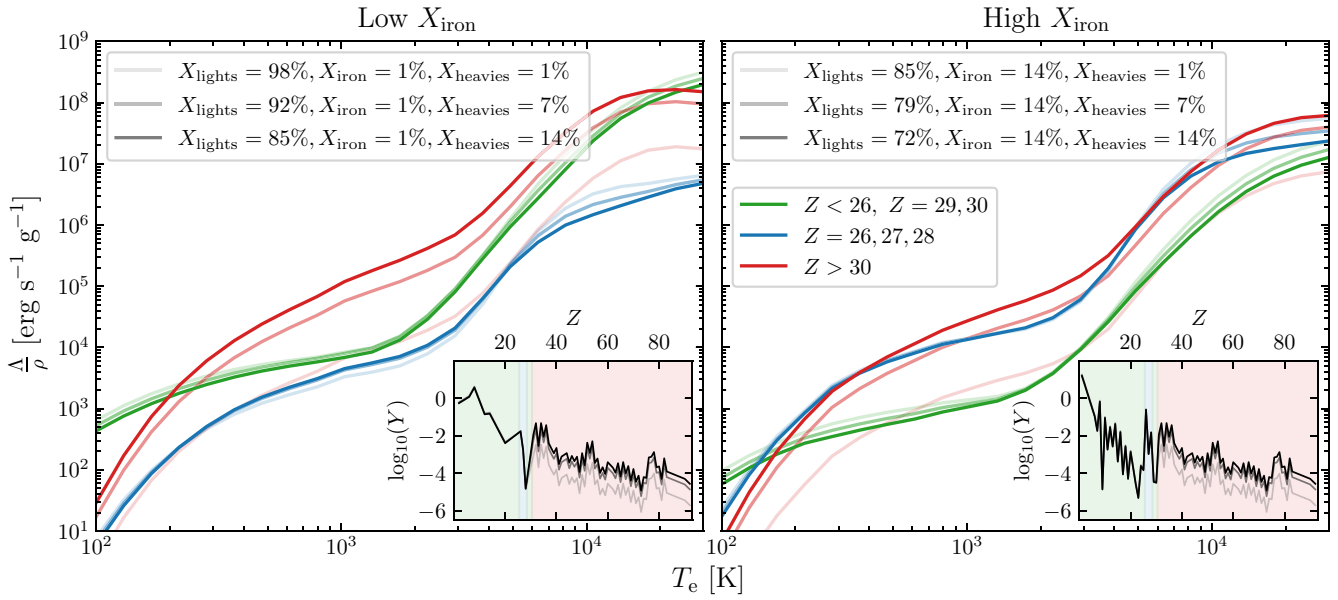

Figure 4. Contribution to the specific cooling coming from light elements ($Z < 26$, $Z = 29, 30$), iron group elements ($Z = 26, 27, 28$) and heavy elements ($Z > 30$), for different mixtures of such groups. The specific cooling rate is shown as a function of the kinetic temperature at a fixed density of 10^6 cm^{-3}, and it is obtained through an iterative computation of the thermal (and ionization) balance. Two sets of variations are considered, i.e. a case with low amount of iron (left panel), and a case with high amount of iron (right panel). For each set, the amount of heavy elements is progressively increased at the expenses of light elements. Each panel also shows the set of correspondent abundance patterns, with the abundance of light elements taken from the S25 model computed by Rauscher et al. (2002) (right panel), and from the r0e2 model computed by Dessart et al. (2017) (left panel), while the abundance of heavy elements being the solar r-process pattern derived by Prantzos et al. (2020).

amount of iron produced, which is in fact higher in, e.g. SN 1998bw, when compared to SN 1987A. Yet, the mass fraction is in this case the determinant factor when investigating the dominance of different species in terms of cooling power within a single zone mixture. From these starting compositions, the fraction of heavy elements is progressively increased from 1 per cent to 7 per cent, and finally to 14 per cent of the total ejecta mass, at the expenses of the light elements. We consider $X_{\rm heavies} = 14$ per cent as a limiting case where the presence of heavy elements is ideally boosted to a rather unrealistic value, for illustrative purposes. For each of the resulting 6 custom compositions, we build the total cooling function of the three elemental groups, by computing ionization and thermal balance over a range of kinetic temperatures and at a fixed density of 10^6 cm^{-3}. The choice of fixing the density is well supported by the fact that the dependence of the cooling function on this parameter is generally minor (Hotokezaka et al. 2021). The thermal balance at each $T_{\rm e}$ is ensured through an iterative process that updates the value of the input heating rate in order to match the total cooling rate.

We show the variation in the different contributions to the cooling associated to the variation in the composition in Fig. 4, with the right panel showing the high $X_{\rm iron}$ case, and the left panel the low $X_{\rm iron}$ case. In absence of heavy elements, iron tends to easily dominate the energy loss, primarily at temperatures from a few hundreds to $\sim 10\,000$ K. Even when the mass of the iron group elements is substantially lowered from 14 per cent to just 1 per cent of the total mass, the iron contribution is still only a factor of a few lower than that of the remaining elements combined, for $T_{\rm e} \sim 1000$ K. The prominent role of Fe, Co, and Ni lines in the nebular phase of SNs is a well established fact, as evidenced by the multitude of observed SN spectra, and especially for Type Ia SNs, where the iron production is even greater.

Yet, in principle, also heavy elements could have a relevant impact, as already pointed out by Hotokezaka et al. (2021) for the KN case, whereas, for example, the cooling efficiency of Nd is more than one order of magnitude greater than that of Fe. In fact, including a full composition, we observe similar cooling rates between heavy elements and iron across a wide range of temperatures, for these two groups having the same mass. In particular, the cooling of heavy elements is more efficient by a factor of a few around $T_{\rm e} \sim 1000$ K, and can be substantially higher also for $T_{\rm e} \gtrsim 10000$ K. In this regard, we note that, at those high temperatures, the cooling function of heavy species may continue to grow with $T_{\rm e}$. However, we observe it saturating instead, likely because we do not model accurately all possible E1 and electric quadrupole (E2) transitions, taking over the M1 ones that instead dominate at lower temperatures. Nevertheless, here we are interested only in the temperature region around a few 10^3 K, where the assumptions of our model are verified.

From our estimates, a few per cent of the total mass in heavy elements is likely sufficient to contribute to the cooling similarly to the entire group of light species. It follows that, depending on the amount of iron, a mass of heavy elements between $\sim$ 1–10 per cent of the total mass is needed in order to observe their overall dominance at a few thousands K. While ejecta with high $X_{\rm iron}$ hardly harbors ~ 10 per cent of the total mass in heavy material, the scenario with lower $X_{\rm iron}$ could produce enough heavy species to, at least partially, become a relevant cooling channel for the ejecta. Still, an absolute dominance of the heavy species over the strong cooling of elements such as O, Ca, or Fe appears unlikely. This result mitigates the roughness of our approximate treatment of E1 transitions in heavy elements, by which the inferred electron temperature and the subsequent M1 spectrum are thus not strongly affected.

We note that the above considerations are obtained by exploring different values for $X_{\rm lights}$, $X_{\rm heavies}$, and $X_{\rm iron}$, under the assumption

that the specific choice of abundance patterns used to characterize the toy elemental mixtures is not crucial in this context. In other words, here we assume that detailed variations in the pattern of the light or of the heavy elements, due to different astrophysical conditions as well as theoretical models, tend to roughly integrate out when computing their total contribution to the cooling rate, on a sufficiently large scale of temperatures. In reality, in a similar fashion to what happens at the nuclear level in the case of the radioactive heating rate, we cannot exclude important contributions from distinguished atomic species to significantly alter the shape of the cooling functions. However, we propose these ballpark estimates as a first step towards the recognition of the role of heavy elements in SNs nebulae.

7 NEBULAR SPECTRA

In addition to the cooling via r-process elements, we investigate their potential imprint on the subsequent spectrum, and its detectability. For this purpose, we choose to target the well studied SN 1998bw, as representative candidate of a scenario where heavy elements may be synthesized.

7.1 Reproducing the late SN 1998bw emission

The nature of SN 1998bw, at a luminosity distance of 37.8 Mpc (Patat et al. 2001), was long debated, due to the intrinsic characteristics of its photometric and spectroscopic evolution. Initially, (Maeda et al. 2003) proposed a stratified ejecta with a slow enough high density core and a fast enough outer shell, each containing ^{56}Ni, in order to explain the emission brightness both at early and late times. This structure has been found difficult to be achieved in spherical symmetry, while it is consistent with more asymmetric explosions. In fact, Dessart et al. (2017) argued that such stratification is not even necessary, once the ejecta asymmetry is exploited. The early phase of the emission could then be explained by a faster component with a relatively higher ^{56}Ni abundance in the polar region, while the later phase would result from a slower component with lower ^{56}Ni concentration along the equator. In any case, the nebular phase is well described by a slow and massive ejecta with a limited amount of ^{56}Ni. The latter is likely more indicative of the true element abundance, when compared to the incredibly highly energetic and ^{56}Ni-rich ejecta necessary to explain, in the spherically symmetric scenario, the first days of emission. This conclusion from Dessart et al. (2017) stems from the analysis of a series of synthetic SN models, post-processed with the time-dependent 1D radiative transfer code CMFGEN (Hillier & Dessart 2012). The models were obtained by evolving a 40 $M_\odot$ ZAMS star with different metallicities and rotation degrees using the stellar evolution code MESA (Paxton et al. 2011, 2015). The resulting carbon-rich WR stars were pushed to explosion with the radiation-hydrodynamics code V1D (Livne 1993; Dessart, Livne & Waldman 2010), in order to obtain ejecta with different kinetic energies.

Here, we use as benchmark for our calculations the r0e2 model from Dessart et al. (2017), which derives from a ZAMS star with no initial rotation and solar metallicity, eventually exploding with a kinetic energy of 4.12×10^{51} erg, and resulting in the best fit of the late observations. Our ejecta are constructed using three concentric zones, with the first representing the innermost region of the outflow, and the third the outermost. As shown in Appendix C, we find that increasing further the number of zones does not lead to an improvement in the final prediction of the spectra, while, conversely, less zones also fail in capturing some of the emergent spectral features. We focus on the observational epochs when we expect our model assumptions to be verified, around the first hundreds of days after the GRB. In particular, among the epochs analysed by Dessart et al. (2017), the one at ~ 215 d appears to be the most suited to represent the conditions corresponding to pure emission nebula.

Table 1. List of relevant quantities characterizing each of the zones in our NLTE model, used to target the SN 1998bw spectra at 215.4 d post-explosion. The values are informed on the r0e2 explosion model from Dessart et al. (2017). From top to bottom, we list the zone total mass $M_{\rm tot}$, average velocity $v_{\rm avg}$, atomic number density n, specific radioactive heating rate $\dot{\epsilon}$, and average atomic mass number $\bar{A}$. We also report the kinetic temperature $T_{\rm e}$ and electron fraction $\chi_{\rm e} = \frac{n_{\rm e}}{n}$, as obtained by running the ionization and thermal balance in each zone.

Zone		1°	2°	3°
$M_{\rm tot}$	($M_\odot$)	1.0	5.8	2.4
$v_{\rm avg}$	(c)	0.007	0.020	0.030
n	(10^7 cm^{-3})	4.88	5.20	0.19
$\dot{\epsilon}$	(10^7 erg s^{-1} g^{-1})	2.56	0.26	0.26
$\bar{A}$		23.1	17.3	14.7
$T_{\rm e}$	(K)	4058	4861	5648
$\chi_{\rm e}$		0.26	0.07	0.30

The main model parameters associated to each zone at this epoch are summarized in Table 1, and are directly informed on the r0e2 model. We also show the correspondent composition in Fig. 5. We note that the mass values reported in Dessart et al. (2017) only include the most relevant elements, such as those that produce observed spectral features. Since the model r0e2 predicts a minor amount of He in the outer layers of the ejecta, we include this element when computing the ionization balance. However, given its low mass, we do not include He lines in the emission model, since it is not observed to play a relevant role in the SN 1998bw spectra. We note that, in any case, generally the presence of a significant amount of He would be recognizable, assuming a Type Ib SN event, through its most prominent emission features, such as the He I line at 5876 Å. At longer wavelengths instead, He could be identified at earlier epochs by the He I P Cygni profiles at 1.08 and 2.06 μm, as found in, e.g. the intermediate Type Ib/c SN 1999ex (Hamuy et al. 2002), or the SN Ic 1994I (Filippenko et al. 1995). Conversely, since the amount of Mg is not reported in Dessart et al. (2017), we include manually this element in the composition, opting for an amount consistent with that of Si, and at the same time able to match the Mg I line at 4571 Å. Since the resulting mass fractions do not add up to 1, we allocate the remaining ejecta mass to a representative average element, that we choose to be Ne. The latter plays an almost inert role in the scope of our work. In particular, it only produces a Ne II line at 12.81 μm, so that the correspondent power relative to the other elements is negligible. Thus, the results of our analysis are not affected by its presence.

The slower innermost zone contains the majority of the total initial ^{56}Ni content, as in the original r0e2 model. However, since our model considers non-thermal heating only from local sources, we slightly redistribute the initial ^{56}Ni, in order to have it in some minor amount also in the other zones, while keeping the total amount fixed to the r0e2 value of ~ 0.12 $M_\odot$. In this way, we roughly mimic the contribution to the emission coming from the outer zones, and powered by the inner one, without including non-local heating rates. At the considered epoch, the energy deposition is governed by the ^{56}Co electron captures and β^+-decays, with the material being still opaque to γ-rays. The latter, and in minor amount also primary positrons, release a few 10^7 erg s^{-1} g^{-1} in the core of the ejecta. As found by computing the ionization and thermal balance in each

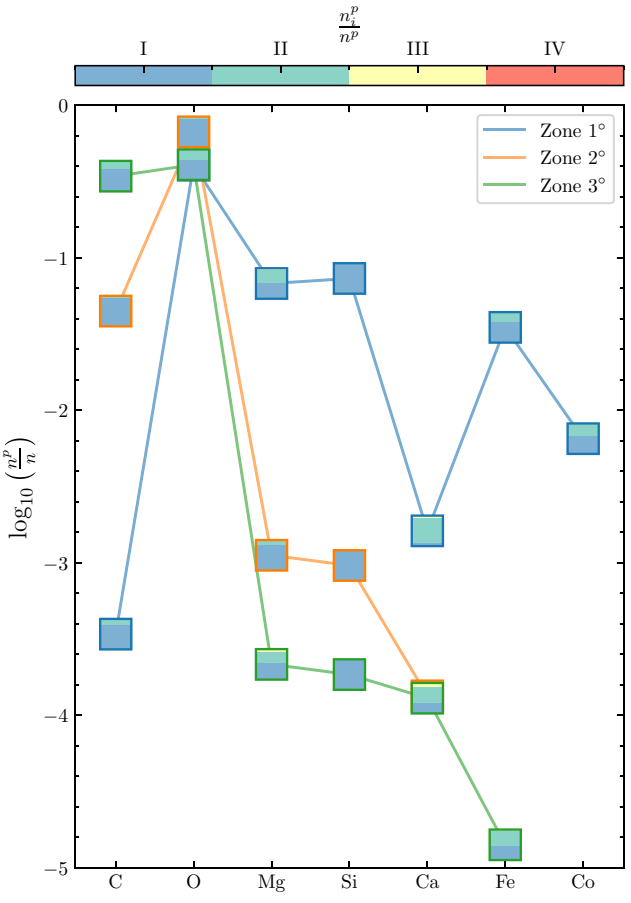

Figure 5. Atomic number fraction $\frac{n^p}{n}$ of the most abundant elements included in our NLTE model, targeted on SN 1998bw at 215.4 d, and informed on the r0e2 model from Dessart et al. (2017). The composition is shown for each of the three constructed zones, and the relative amount of the different ionization stages $\frac{n_i^p}{n^p}$, as obtained from ionization and thermal balance, is displayed for each element as a stacked histogram.

zone, this energy is spent to ionize matter more efficiently in the outer layer, due to the lower density. The resulting kinetic temperature and ionization stage are the highest in the third zone, as shown in Table 1 and Fig. 5, respectively. In this region, many species are relevantly ionized to the second stage, including Fe, and up to the third stage in the case of Mg and Ca. Note that in this model the intermediate zone is instead the one with the lowest average ionization stage. This is because the matter density is only slightly lower than the first zone, while the average atomic mass decreases relevantly, leading to a higher number density of atoms (see Table 1). On the other hand, the lighter composition releases the input heating at higher temperatures, in absence of the strong Fe cooler, causing the kinetic temperature to monotonically increase from the core to the surface of the ejecta.

We compare in the lower panel of Fig. 6 the resulting optical spectrum with the r0e2 model, and with the SN 1998bw observation (corrected for extinction and redshift) at ~ 215 d after the GRB (~ 201 d after B maximum light), from the coverage done by the European Sourthern Observatory (ESO) on La Silla and VLT/UT1 on Paranal (Sollerman et al. 2000; Patat et al. 2001). The contributions to the emission coming from the different atomic species are displayed cumulatively, so that their combination is directly comparable with the r0e2 model and the observation. Both the r0e2 and our model are rescaled to match the feature at ~ 6300 Å. The latter, corresponding to the O I forbidden doublet at 6300–6363 Å, is the most prominent feature of this nebular spectrum, generated within the outer core of the ejecta (second zone in the model), and appearing already tens of days before the considered epoch. The presence of such line, together with the narrower Mg I line at 4571 Å, and the Ca II doublet at 7300 Å (produced in the first zone), are consistent with what observed in several spectra from Type Ib/c SNs, such as the SNs Ic 1987M and 1996aq, and the SN Ib 1996N (see, e.g. Patat et al. 2001, for a direct comparison of these events). The relative strength of the above features is in agreement with what found by Dessart et al. (2017) with the r0e2 model, even though both the synthetic spectra fail in reproducing the absolute strength of the Ca II line at 7300 Å. Given the abundance of Ca II, a strong line from its triplet at 8498–8542 − 8662 Å would be also expected, but it is missing, due to it being mostly populated through absorption. Instead, we find a broad feature from the C I forbidden triplet at 8730 Å, that emerges from the outer ejecta layer (third zone).

Regardless of the Mg I line at 4571 Å, the region of bluer wavelengths $\lesssim 5500$ Å, which in our model is dominated by a series of Fe I lines from the ejecta core, is poorly reproduced. Possibly, in this range at ~ 215 d, there is still a residual continuum inherited from the past epochs, as it can be inferred by comparing the correspondent earlier spectra. For example, the spectrum at ~ 108 d (upper panel of Fig. 6) presents an evident underlying continuum, that extends up to the O I line and beyond. As expected, our model is practically unable to reproduce the observed spectrum in such case, since it does not consider any continuum radiation, nor absorption effects other than self-absorption. The absence of the latter effects, and in particular of Fe blanketing, could be a concurrent reason for the apparently overestimated Fe I emission flux, whereas, in the same wavelength range, Dessart et al. (2017) argue for the presence of a forest of Fe II and Ti II lines, together with Ca II absorptions. However, while singly ionized atoms are present in somewhat comparable amounts to the neutral atoms for most of the included elements, the absence of strong Fe II lines in particular also suggests a possible underestimation of the ionization processes. In fact, we model ionization due to non-thermal electrons and recombination photons from the ground states, but we do not include ionization from the excited states, which could significantly enhance the ionization rates of neutral ions. We investigate in Section 7.3 the impact that our uncertainty on the degree of ionization has on our estimates for the r-process signatures in the spectra.

Despite the clear limitations due to the absence of an implementation of radiative transfer and the partial treatment of all the relevant atomic processes, the comparison with the spectra of SN 1998bw highlights that our model is able to, at least approximately, reproduce some distinctive traits of late SN Ib/c emissions. We therefore take these features as references in order to explore the injection of species heavier than Fe group elements in the SN ejecta.

7.2 r-process signatures in the spectra

We start from the model constructed in Section 7.1, and we progressively introduce heavy elements ($Z > 30$) into the composition. For the relative abundance of such species, we adopt the solar r-process pattern from Prantzos et al. (2020), and for simplicity, we add the same mass of r-process elements to all the zones simultaneously (see Section 7.3 for a discussion on the impact of this assumption), at the expenses of our inert element, i.e. Ne. In this way, our modification of the composition does not affect the masses of the relevant lighter elements, nor their relative abundance. We show in Fig. 7 the spectra

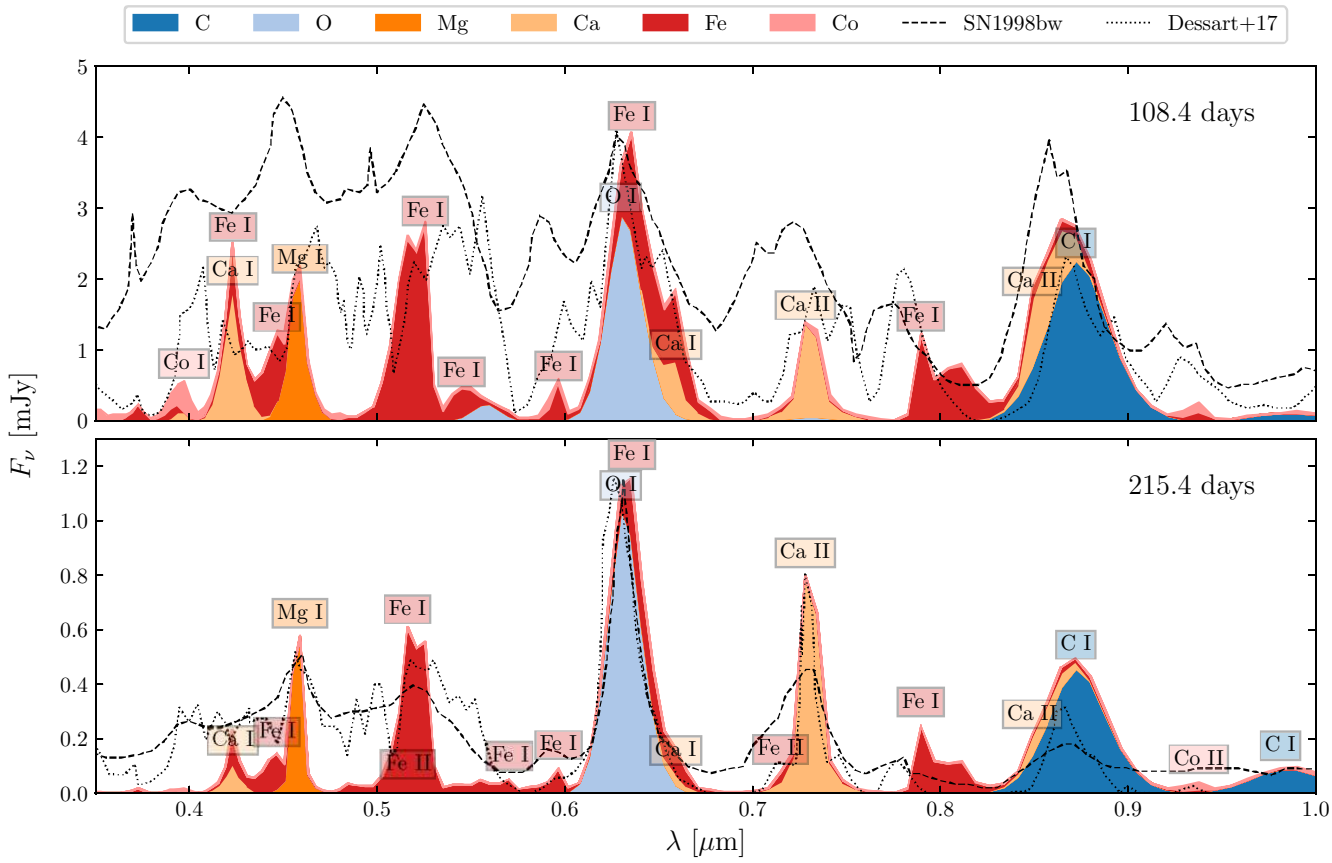

Figure 6. Optical to near-IR spectra computed with our NLTE model at 108.4 and 215.4 d post-explosion, compared to the observed spectra of SN 1998bw, corrected for redshift and extinction (dashed line). The r0e2 model from Dessart et al. (2017) is also shown for comparison. Both models are normalized to the observed feature at $\sim$ 6300 Å dominated by the O I forbidden doublet. The relevant contributions of the included elements to the total flux are shown by colour-coding with respect to the element and stacking them according to increasing Z, while the specific ion species responsible for the features are explicitly noted.

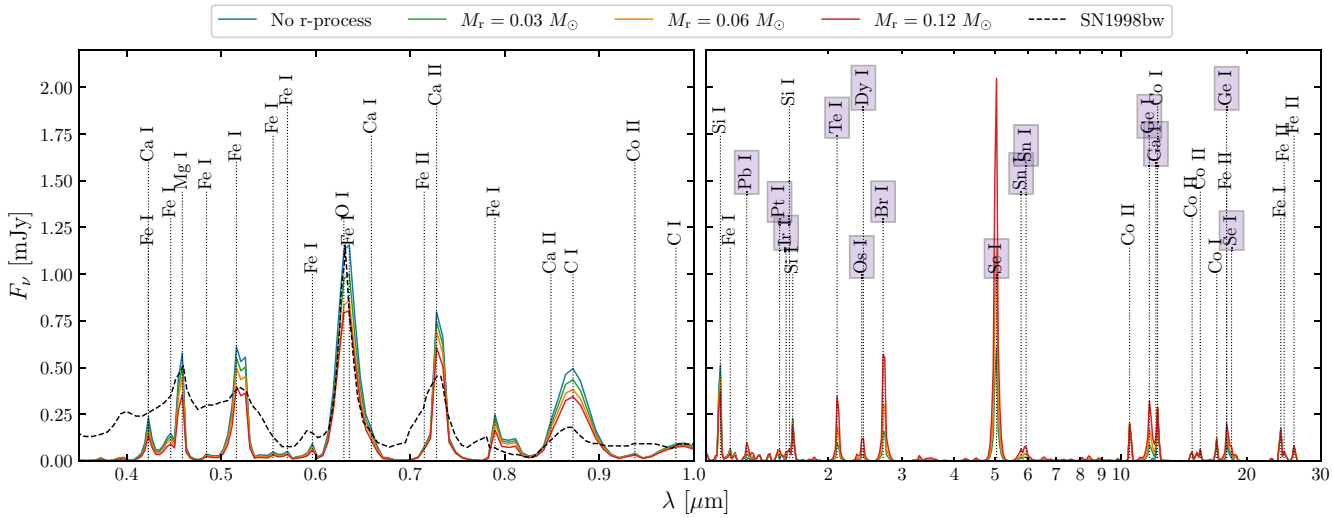

Figure 7. Optical to mid-IR spectra computed with our NLTE model targeted on SN 1998bw at 215.4 d post-explosion, for different amounts of r-process material included in the modelled composition. The observed SN 1998bw spectra, corrected for redshift and extinction, is shown as reference (dashed line). The ion species responsible for the most relevant features are explicitly noted, with the new species with $Z \geq 30$ highlighted with boxes.

resulting from the inclusion of a mass of r-process elements M_r varying from zero to 0.12 $M_\odot$, which is roughly the amount of the initial ^{56}Ni content. In the absence of heavy elements, the emission flux is mostly concentrated at shorter wavelengths, in the optical region. On the other hand, with our current transition list, heavy elements generate forbidden lines in the near/mid-IR. The near-IR excess caused by their presence has been already suggested in several works before (see e.g. Siegel et al. 2019). Here, in order to quantify

Table 2. Total energy flux on Earth from a SN 1998bw-like event (at a luminosity distance of 37.8 Mpc, 215.4 d post-GRB), for different amounts of r-process elements mass M_r included in the composition. Fluxes are computed separately for the wavelength ranges ≤ 1 μm and > 1 μm, and their ratio $R_F = \frac{F_{>1\ \mu m}}{F_{\leq 1\ \mu m}}$ is shown to quantify the effect of the inclusion of heavy elements.

M_r [$M_\odot$]	$\frac{M_r}{M_{ej}}$	$\frac{M_r}{M_{^{56}Ni}}$	$F_{\leq 1\ \mu m}$ $\times 10^{-13}$ (erg s^{-1} cm^{-2})	$F_{>1\ \mu m}$ $\times 10^{-13}$ (erg s^{-1} cm^{-2})	R_F
0.00	0.000	0.00	7.22	0.54	0.08
0.03	0.003	0.25	6.40	0.73	0.11
0.06	0.007	0.50	5.65	0.90	0.16
0.12	0.013	1.00	4.88	1.23	0.25

it, we integrate the flux in the wavelength range ≤ 1 μm, and the flux in the range > 1 μm, that is $F_{\leq 1\ \mu m}$ and $F_{>1\ \mu m}$, respectively. We compare the two fluxes by referring to their ratio $R_F = \frac{F_{>1\ \mu m}}{F_{\leq 1\ \mu m}}$ in Table 2. Since we used Ne as our inert species, when computing the spectra (displayed in Fig. 7) and the total fluxes, we ignore the Ne II line at 12.81 μm. In doing so, we assume that the residual mass which we do not account for does not change the values of R_F significantly.

As visible in Fig. 7, in absence of elements heavier than iron group ones, we observe a flux ratio $R_F \sim 10^{-1}$. Specifically, besides the already mentioned features in the optical, in the near/mid-IR we find lines of Fe I and Si I between 1 and 2 μm, and lines of Fe I and II, and Co I and II, between 10 and 30 μm. The first new lines that appear, once a relatively small amount of heavy elements is included in the composition (0.3 per cent of the total mass), are from Te I at 2.10 μm, Br I at 2.71 μm, Se I at 5.03 μm, and Ge I at 11.73 μm. In particular, the line from Se I, here the strongest feature in the mid-IR range, appears relevant also in recent KN nebula calculations from Banerjee et al. (2025). The latter, as well as the ones from Ge I and Br I, are considerably difficult to interpret, due to the alternative nucleosynthetic pathways available for the production of such elements. The consensus of the community on the subject is still in general disarray, whereas it is not clear if these elements can be created also in normal SNe. Instead, the prompt appearance of the line from Te I (here with significant strength of ~ 0.1 mJy at the considered distance), originating from the M1 + E2 transition $5p^4\ ^3P_1 - 5p^4\ ^3P_2$, would be a good indicator for an r-process which creates second peak elements.

A few times 0.01 $M_\odot$ of r-process material are sufficient for the Te I line at 2.10 μm to have a strength comparable to that of the Si I lines at 1.10 μm and 1.65 μm. In Type Ic SN events, such as SN Ic 2007gr (Hunter et al. 2009), or SN Ic 2022jli (Cartier et al. 2024), the above Si I features have been identified, while there is no evidence for similarly strong lines around 2.1 μm. On this basis, we can thus place a constraint on the amount of r-process material produced in events of this kind. We consider, for example, SN 2007gr, which, at ~ 176 d past B maximum light, shows a luminosity $\Delta_\lambda L_\lambda \sim 9 \times 10^{37}$ erg s^{-1} around ~ 2 μm (Hunter et al. 2009). If we assume temperature and density conditions similar to those found in our model for SN 1998bw ($T_e \sim 4000$ K, $n_e \sim 10^7$ cm^{-3}), we expect Te atoms to be mostly neutral and in the ground state, and the line at 2.1 μm to be dominated by radiative de-excitations. In this limit, the luminosity of the line can be approximated by

$$\Delta_\lambda L_\lambda = N_{Te} E_\lambda n_e k_\lambda\,, \tag{20}$$

with N_{Te} the number of Te atoms, and k_λ the collisional excitation rate coefficient of the line. If we interpret the observed luminosity around ~ 2 μm as a limit to the Te I line luminosity, we can invert equation (20) to find a maximum amount of Te atoms, and by extension of r-process material:

$$M_r \lesssim \left(\frac{\Delta_\lambda L_\lambda}{5 \times 10^{41}\ \mathrm{erg\ s^{-1}}}\right)\left(\frac{X_{r,Te}}{0.03}\right)^{-1}\left(\frac{n_e \Omega_\lambda}{10^7\ \mathrm{cm^{-3}}}\right)^{-1} M_\odot\,. \tag{21}$$

Here, $X_{r,Te}$ is the mass fraction of Te relative to the r-process composition, with 0.03 its value in the case of the solar r-process pattern (Prantzos et al. 2020), while Ω_λ is the collision strength of the Te I line (~ 1 in our calculations). In the case of SN 2007gr, assuming the values proposed in equation (21), we thus obtain a stringent limit to the r-process mass $M_r \lesssim 2 \times 10^{-4}\ M_\odot$.

Injecting 0.06 $M_\odot$ of r-process content in our SN 1998bw model composition causes the emergence of small features from Dy I and Pb I between 1 and 3 μm. Doubling this amount makes the flux in the same wavelength range to be enriched in small part also by Os I, Ir I, and Pt I lines. These additional contributions from third peak elements appear only for a total mass of r-process material which is comparable to that of ^{56}Ni. Since this is already a rather optimistic scenario, both in terms of r-process production and source distance, we expect that the potential detection of third peak r-process elements is in any case more difficult, compared to that of second peak elements.

Regardless, it appears clear that there is a systematic shift of the overall flux towards longer wavelengths, the more heavy elements are included (assuming our line list to be complete enough). In the most extreme case considered, $F_{>1\ \mu m}$ reaches even a fourth of the optical part. According to these estimates, we can therefore expect that the presence of heavy elements in the ejecta from this type of SNs may be already hinted by a value of R_F which is greater than ~ 0.1. Clearly, the presence of r-process elements in events which are further away, compared to a few tens of Mpc, will prove more difficult to be deciphered. However, the sensitivity limit of the new *JWST* instrumentation in, e.g. 1–3 μm with the NIRSpec and the NIRCam is of the order of ~ 0.1–10 μJy, allowing for a much deeper search (up to hundreds of Mpc) of such revealing features in the spectra. We therefore list in Table 3 the most relevant forbidden lines from heavy elements, which, according to our model, could potentially be used as reference for the identification of r-process signatures. We note that this list does not include possible E1 lines from neutral or mildly ionized heavy species which may be important as well, depending on the conditions, as we do not include the related processes in our modeling. In fact, a residual continuum could populate the energy levels corresponding to these lines at similar or shorter wavelengths, as it was already considered in the case of KNs, with the absorption features by, e.g. Sr II at 1.00, 1.03, 1.09 μm (Watson et al. 2019; Domoto et al. 2021), or La III at 1.39, 1.41 μm and Ce III at 1.58, 1.60, 1.61 μm (Domoto et al. 2022; Tanaka et al. 2023), or in the case of stellar mergers, with, e.g. Rb I at 0.78, 0.79 μm and Cs I at 0.85, 0.89 μm (see e.g. Kamiński et al. 2015). We expect these features to be an equally interesting channel via which potentially identifying the presence of heavy elements alongside the forbidden lines.

7.3 Robustness of the results

While in Section 7.2 we adopted a homogeneous distribution of the r-process material across the ejecta, we note that in general this assumption may not hold. In fact, in the case of collapsars, the material undergoing r-process is thought to flow out of the

Table 3. List of first forbidden lines from heavy elements ($Z > 30$) that appear as a solar r-process composition is injected (as in Fig. 7). For each line, we report the parent ion, the transition wavelength λ, and the upper and lower level of the transition, with their energy $E_{\rm upper}$ and $E_{\rm lower}$, respectively. We include both the lines featured in our SN 1998bw model, and additional or alternative lines appearing should the overall ionization degree of the composition be increased (as investigated in Section 7.3).

Ion	λ (Å)	$E_{\rm upper}$ (cm^{-1})	$E_{\rm lower}$ (cm^{-1})	Upper level	Lower level
Ga I	121 037.536	826.190	0.000	$3d^{10}\,4s^2\,4p\,^2P^o_{3/2}$	$3d^{10}\,4s^2\,4p\,^2P^o_{1/2}$
Ge I	117 257.105	1409.961	557.134	$4s^2\,4p^2\,^3P_2$	$4s^2\,4p^2\,^3P_1$
Ge I	179 490.004	557.134	0.000	$4s^2\,4p^2\,^3P_1$	$4s^2\,4p^2\,^3P_0$
Ge II	56 581.665	1767.357	0.000	$4s^2\,4p\,^2P^o_{3/2}$	$4s^2\,4p\,^2P^o_{1/2}$
As III	34 013.606	2940.000	0.000	$4s^2\,4p\,^2P^o_{3/2}$	$4s^2\,4p\,^2P^o_{1/2}$
Se I	50 263.962	1989.497	0.000	$4s^2\,4p^4\,^3P_1$	$4s^2\,4p^4\,^3P_2$
Se I	183 532.377	2534.360	1489.497	$4s^2\,4p^4\,^3P_0$	$4s^2\,4p^4\,^3P_1$
Se III	45 537.341	3937.000	1741.000	$4s^2\,4p^2\,^3P_2$	$4s^2\,4p^2\,^3P_1$
Se III	57 438.255	1741.000	0.000	$4s^2\,4p^2\,^3P_1$	$4s^2\,4p^2\,^3P_0$
Se IV	22 851.920	4376.000	0.000	$4s^2\,4p\,^2P^o_{3/2}$	$4s^2\,4p\,^2P^o_{1/2}$
Br I	27 135.275	3685.240	0.000	$4s^2\,4p^5\,^2P^o_{1/2}$	$4s^2\,4p^5\,^2P^o_{3/2}$
Br II	31 883.689	3136.400	0.000	$4s^2\,4p^4\,^3P_1$	$4s^2\,4p^4\,^3P_2$
Br IV	33 445.935	5611.900	2622.000	$4s^2\,4p^2\,^3P_2$	$4s^2\,4p^2\,^3P_1$
Br IV	38 138.826	2622.000	0.000	$4s^2\,4p^2\,^3P_1$	$4s^2\,4p^2\,^3P_0$
Kr II	18 621.627	5370.100	0.000	$4s^2\,4p^5\,^2P^o_{1/2}$	$4s^2\,4p^5\,^2P^o_{3/2}$
Kr III	21 985.753	4548.400	0.000	$4s^2\,4p^4\,^3P_1$	$4s^2\,4p^4\,^3P_2$
Rb III	13 560.242	7374.500	0.000	$4s^2\,4p^5\,^2P^o_{1/2}$	$4s^2\,4p^5\,^2P^o_{3/2}$
Pd II	28 254.638	3539.242	0.000	$4d^9\,^2D_{3/2}$	$4d^9\,^2D_{5/2}$
Pd III	30 966.464	3229.300	0.000	$4d^8\,^3F_3$	$4d^8\,^3F_4$
Sn I	57 608.101	3427.673	1691.806	$5s^2\,5p^2\,^3P_2$	$5s^2\,5p^2\,^3P_1$
Sn I	59 108.433	1691.806	0.000	$5s^2\,5p^2\,^3P_1$	$5s^2\,5p^2\,^3P_0$
Sn II	23 521.144	4251.494	0.000	$5s^2\,5p\,^2P^o_{3/2}$	$5s^2\,5p\,^2P^o_{1/2}$
Te I	21 049.477	4750.712	0.000	$5p^4\,^3P_1$	$5p^4\,^3P_2$
Te III	21 048.201	4751.000	0.000	$5s^2\,5p^2\,^3P_1$	$5s^2\,5p^2\,^3P_0$
Te III	29 291.155	8165.000	4751.000	$5s^2\,5p^2\,^3P_2$	$5s^2\,5p^2\,^3P_1$
Dy I	24 188.348	4134.222	0.000	$4f^{10}\,6s^2\,^5I_7$	$4f^{10}\,6s^2\,^5I_8$
Os I	24 042.392	4159.320	0.000	$5d^6\,6s^2\,^5D_3$	$5d^6\,6s^2\,^5D_4$
Os II	27 830.734	3593.150	0.000	$5d^6\,(^5D)\,6s\,^6D_{7/2}$	$5d^6\,(^5D)\,6s\,^6D_{9/2}$
Os III	25 979.020	3849.260	0.000	$5d^6\,^5D_3$	$5d^6\,^5D_4$
Ir I	15 813.002	6323.910	0.000	$5d^7\,6s^2\,^4F_{7/2}$	$5d^7\,6s^2\,^4F_{9/2}$
Pt I	15 226.606	6567.452	0.000	$5d^9\,6s\,^3D_2$	$5d^9\,6s\,^3D_3$
Pb I	12 788.930	7819.262	0.000	$6s^2\,6p^2\,\left(\frac{3}{2}\,\frac{1}{2}\right)_1$	$6s^2\,6p^2\,\left(\frac{1}{2}\,\frac{1}{2}\right)_0$

accretion disk formed by the circularized star core, provided its neutronization being efficient (Siegel et al. 2019). In such a scenario, the r-process material could be concentrated in the inner region of the ejecta, spatially separated from the lighter material. Yet, the variability associated to the event, as well as the uncertainties in its modelling, may result in very different distributions of r-process content within the ejecta, as well as a variable degree of mixing with the lighter species (Barnes & Metzger 2022; Barnes & Duffell 2023). In light of these considerations, we explore the effect of the r-process spatial distribution in Fig. 8 for our model with $M_{\rm r} = 0.03\,{\rm M}_\odot$. If we inject the entire amount of heavy elements in the inner zone alone, corresponding to the ejecta core, the production of the same lines is boosted by the larger heating rates. At the same time, the ejecta conditions across the modelled zones are not sufficiently different to alter significantly the average ionization stage of such species. On the other hand, we also consider the case in which the r-process material is contained within a pocket spatially separated from the rest of the composition. We obtain this scenario by adding a fourth zone to our model, sharing the same conditions as the original inner zone, but containing only the r-process material, in order to leave intact the composition profiles of the lighter species. In such a scenario, the lines from r-process elements may still be present, but with a considerably reduced strength, due to the fact that the heating by the sole r-process is much lower than that from the ^{56}Ni radioactivity. This result depends heavily on our modelling, whereas we treat only a local heating source. Since in general we can imagine the r-process pocket to be potentially heated also by neighbouring regions, we can consider the above case as a lower limit to the expected strength

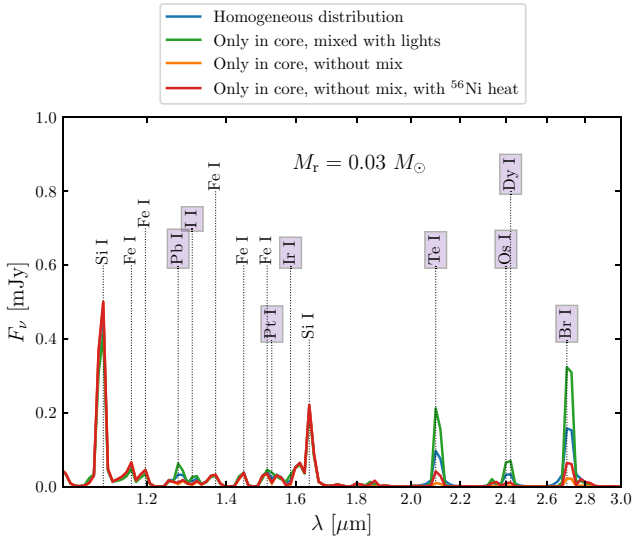

Figure 8. Zoom in the near-IR of the spectrum shown in Fig. 7 for the model with $M_r = 0.03$ M$_\odot$, obtained by injecting heavy elements uniformly in all zones (homogeneous distribution). For comparison, the model with the same mass of heavy elements concentrated only in the inner zone (core), which still contains also lighter species, is shown. The case in which the heavy elements are spatially separated from the lighter ones is also displayed, with and without external heating from the ^{56}Ni chain radioactivity.

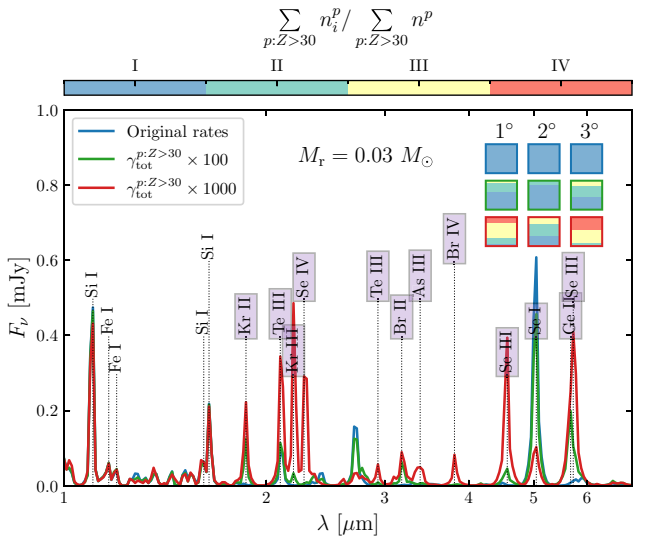

Figure 9. Zoom in the near to mid-IR of the spectrum shown in Fig. 7 for the model with $M_r = 0.03$ M$_\odot$, compared to the same model where the total ionization rate of heavy elements ($Z > 30$) is systematically boosted of a factor 100 and 1000. For every model, the total ionization fractions of these heavy elements in each zone are shown as stacked histograms (top right of the figure).

of the r-process lines. As a rough reference for the opposite limit instead, Fig. 8 also shows the case in which the r-process pocket receives heat from 0.003 M$_\odot$ of ^{56}Ni (i.e. the same mass fraction of the inner light elements zone). As expected, this case results in strengths of the same features which are intermediate between the scenarios described above. As a consequence, the argument exposed in Section 7.2 on the detectability of heavy elements, generally holds regardless of their distribution within the ejecta, as long as the r-process material is heated enough to produce lines in the first place. We note, however, that this conclusion is aided by the assumption that the medium is optically thin, whereas the emitted lines are not reprocessed in other ejecta regions. Furthermore, we acknowledge that our treatment of ionization and recombination itself is affected by potentially large uncertainties, both due to the atomic data, and due to the atomic and thermodynamic processes neglected. As seen in Section 7.1, the achieved ionization stage of lighter elements is in rough agreement with what it is observed in SN 1998bw, despite some difficulties in accurately reproducing the high frequency features still remain. On the other hand, the ionization state of heavier elements is less constrained, and it could be affected by them being to some degree clumped within the ejecta.

We thus explore how our findings would change, assuming the case in which our modeling, or alternative underlying ejecta conditions, would result in a different overall ionization stage of the system. Fig. 9 shows the model with $M_r = 0.03$ M$_\odot$, where the total ionization rate for the heavy elements ($Z > 30$) is increased artificially, first by a factor 100, and then 1000. In the first case, singly ionized species appear in the composition in amounts comparable to the neutral species, with the most relevant new lines being from Kr II at 1.86 μm, Br II at 3.19 μm, and Ge II at 5.66 μm. In the second case, boosting the ionization of heavy species further, we obtain a large part of the population to be in the third and even fourth ionization stage. In such a scenario, we observe the Te I line at 2.10 μm being substituted by the Te III line at the same wavelength, already found by Hotokezaka et al. (2023) in the nebular phase of the KN AT2017gfo. With similar strengths, also Kr III and Se IV produce observable lines, respectively at 2.20 and 2.29 μm. At longer wavelengths instead, Se III dominates with two lines at 4.55 and 5.74 μm, taking the place of the Se I line at 5.03 μm. Furthermore, additional smaller features are generated by Te III, As III, and Br IV, at 2.93, 3.40, and 3.81 μm, respectively.

Compared to the results obtained with the original ionization rates, we note that the different ionization stage of the system results in the most prominent features from neutrals being substituted by similarly strong features from their ionized counterparts, at similar wavelengths. In particular, the elements originally producing the most relevant lines continue to characterize the near to mid-IR spectrum, with the possible addition of Kr and As. As such, the spectrum remains shaped by the lighter heavy elements with Z = 32–36, which are co-produced via different channels, and by Te, which continues to be potentially detectable, assuming the material in the line forming region at the considered epoch being not too fast. We include in Table 3 the additional lines found by varying the overall ionization stage for different amounts of r-process material.

On a different note, however, we have to consider the possibility that the wavelength region of interest could be in general polluted by additional lines emerging from recombination photons. For this reason, here we give an estimate for their potential presence, using data available in literature. We model the recombination spectrum in a similar way to equation (14), that is

$$L_\nu = \sum_{m,l:m>l} N_m E_{ml} n_e \alpha_{ml} \mathcal{N}_\nu \left(\nu_{ml}, \left(\frac{\nu_{ml} v}{\sqrt{2}c} \right)^2 \right) , \tag{22}$$

where the sum runs over the lines emitted from excited levels m into which the atoms recombine with a rate α_m. The latter is used to compute the line rate coefficient

$$\alpha_{ml} = \frac{A_{ml}}{\sum_{n:m>n} A_{mn}} \alpha_m , \tag{23}$$

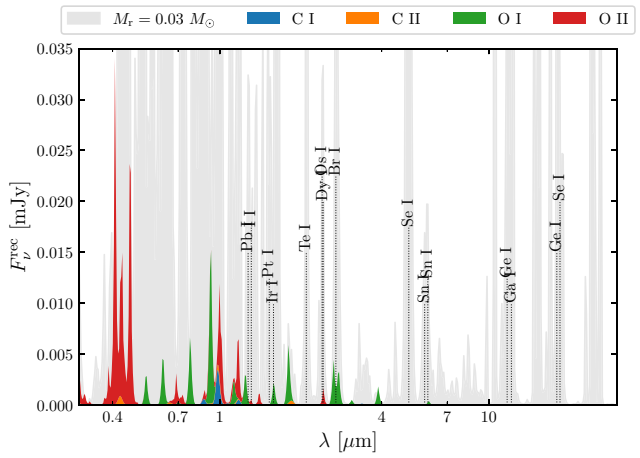

Figure 10. Recombination spectrum obtained for the composition and the ejecta conditions reported in Fig. 5 and Table 1, respectively. The contributions from the relevant ion species are colour-coded and stacked to form the total flux. The grey background spectrum, and the relative most relevant heavy ion species noted, correspond to the model with $M_r = 0.03\ M_\odot$, shown in Fig. 7.

which accounts for the branching to different lower states. We include the relevant lines from the species responsible for most of the recombination events, by importing level-specific recombination rates for C I from Nahar (1995a), C II from Davey, Storey & Kisielius (2000), O I from Nahar (1999), O II from Storey (1994), and Mg I and Si I from Nussbaumer & Storey (1986).

As shown in Fig. 10 for the model with $M_r = 0.03\ M_\odot$, C and O are the only relevant contributors to the recombination spectrum, with O I being the dominant source in the optical region, while the near-IR being mainly occupied by O I and II lines. Using the parameters of the zones in the models considered above, we obtain a total recombination photon flux which is more than one order of magnitude smaller than the flux of photons from collisionally excited atoms, both in the optical and in the IR range. In this regard, we note that shifts in the current lines, as well as the appearance of additional lines, could potentially emerge from the employment of a more complete and precise data set. However, we expect the overall strength of such features to be comparable with our current estimates, given the same ejecta conditions. This result justifies the fact that we do not calculate the spectrum of recombination photons including it in the overall thermal balance of the system, and suggests that the lines from heavy elements in the near/mid-IR range should remain detectable.

8 CONCLUSION

Here, we proposed an estimate of the impact that r-process elements are expected to have in the emergence of the optical to mid-IR nebular emission from the ejecta of an SN event. The latter must be peculiar enough in order to harbor the nucleosynthesis of such species, as it could potentially occur in a MR SN or a collapsar. Among the different classes of SNs, GRB SN (BL Type Ic) point to the above scenario, being more energetic, and featuring a relativistic jet. We therefore referred to a representative event, SN 1998bw, modelling its nebula a few hundreds days post-explosion. The model employed solves the ionization, atomic level, and thermal balance, in an approximate way, by assuming the ejecta to be optically thin throughout its depth, and in a steady-state regime, where atomic processes are fast compared to the dynamical time-scale. We therefore study the epochs that proceed from the photospheric phase of the explosion, but are well contained within the first couple of years. This simplification allows for the inclusion of an arbitrary number of elemental species, which we characterize using the atomic data mostly available in public data bases. Unfortunately, for a list of elements including r-process products, such data are still largely incomplete, which introduces a further source of uncertainty in the model. However, the generality of our estimates makes them rather independent on the quality of the atomic data employed, whereas variations, e.g. on the recombination rates should lead to similar detectability conclusions.

Starting from these assumptions, we first explored the overall role of r-process elements in heating and cooling the ejecta. We noted that for typical masses of ^{56}Ni and ^{44}Ti, consistent with the kind of explosions considered, $\sim 10^{-2}$ $M_\odot$ of r-process material could potentially leave a mark only at a very late stage of the light curve, around ~ 10 yr, in the form of a different decay slope. However, this evidence could be very well polluted by the presence of additional energy sources, and to a minor extent also by the less constrained ^{57}Ni. On the other hand, at least in the steady-state phase of the nebula, we found that the same amount of heavy elements is not likely sufficient to impact its cooling process. Despite the greater cooling efficiency expected for single heavy elements such as Nd, the large presence of lighter elements like O, Ca, and up to Fe, requires the heavier species to constitute at least ~ 1 per cent of the total ejected mass, in order to contribute relevantly to the cooling rate. In addition, a non-trivial dependence on the kinetic temperature is retained, due to the different atomic structure and consequent transition lines of such species.

However, targeting the representative case of SN 1998bw, we also found that the near to mid-IR range of the emission spectrum leaves room for heavy elements to be possibly detected regardless, due to the both minor and cleaner emission from lighter species, compared to the optical range. This result appears rather solid even in relation to the potential pollution by lines from recombined ions, and to a good extent for different heavy elements distributions within the ejecta. For example, in the specific case considered, a few times 10^{-2} $M_\odot$ of solar-type r-process material (corresponding to a few 0.1 per cent of the ejecta mass) could leave a signature in the form of a line of Te I at 2.10 μm. Thus, this feature could be used as smoking gun for the occurrence of a relatively strong r-process, or, conversely, its absence could be used to constrain the produced amount of r-process elements. For example, in the case of SN 2007gr, we estimated an r-process mass limit of $M_r \lesssim 2 \times 10^{-4}$ $M_\odot$. Alternatively, a line from Te III at the same wavelength could still serve the same purpose, in the hypothesis that the uncertainties in our modelling would substantially affect our estimates, and we would strongly underestimate the overall ionization stage. On a different note, independently from the identification of single elemental species, a general hint for the presence of r-process elements could be the ratio between near to mid-IR and optical flux, because of the overall asymmetry in the cooling frequencies of light and heavy elements. We estimated such ratio to be above ~ 0.1, in order to be significantly linkable to the presence of heavy elements.

In conclusion, considering the new observational capabilities of *JWST*, we expect the detection of r-process elements to be realistically feasible, especially by focusing the search efforts in a wavelength interval comprised between $\sim$ 1–10 μm. The presence (or absence) of such species in the ejecta from special type of SNs would then provide a tremendous assist to the comprehension of these events, shedding light over the mechanisms responsible for the explosion and the subsequent nucleosynthesis. Ultimately, *JWST*

observations will prove essential for the understanding of the origin of heavy elements in the Universe.

ACKNOWLEDGEMENTS

We thank Anders Jerkstrand, Brian Metzger, and Masaomi Tanaka for useful discussions. This work is supported by the Deutsche Forschungsgemeinschaft (DFG, German Research Foundation, Project ID 279384907, SFB 1245), the State of Hesse within the Research Cluster ELEMENTS (Project ID 500/10.006), the JST FOREST Programme (JPMJFR2136), and the JSPS Grant-in-Aid for Scientific Research (20H05639, 20H00158, 23H01169, 23H04900). CHIANTI is a collaborative project involving George Mason University, the University of Michigan (USA), University of Cambridge (UK), and NASA Goddard Space Flight Center (USA).

DATA AVAILABILITY

The data concerning this work will be shared on reasonable request to the authors.

REFERENCES

Abbott B. P. et al., 2017a, Phys. Rev. Lett., 119, 161101
Abbott B. P. et al., 2017b, ApJ, 848, L12
Anand S. et al., 2024, ApJ, 962, 68
Axelrod T. S., 1980, PhD thesis, California University, Santa Cruz
Badnell N. R., 1986, J. Phys. B: Atom. Mol. Phys., 19, 3827
Badnell N. R., 2006, ApJS, 167, 334
Bahcall J. N., Wolf R. A., 1968, ApJ, 152, 701
Banerjee S., Jerkstrand A., Badnell N., Pognan Q., Ferguson N., Grumor J., 2025, preprint(arxiv:2501.18345)
Bar-Shalom A., Klapisch M., Oreg J., 2001, J. Quant. Spectrosc. Radiat. Transfer, 71, 169
Barnes J., Duffell P. C., 2023, ApJ, 952, 96
Barnes J., Kasen D., 2013, ApJ, 775, 18
Barnes J., Metzger B. D., 2022, ApJ, 939, L29
Barnes J., Kasen D., Wu M.-R., Martinez-Pinedo G., 2016, ApJ, 829, 110
Barnes J., Duffell P. C., Liu Y., Modjaz M., Bianco F. B., Kasen D., MacFadyen A. I., 2018, ApJ, 860, 38
Bautista M. A., 2004, A&A, 420, 763
Beniamini P., Piran T., 2024, ApJ, 966, 17
Bhatia A. K., Kastner S. O., 1995, ApJS, 96, 325
Bleda E. A., Altun Z., Badnell N. R., 2022, A&A, 668, A72
Blondin S., Dessart L., Hillier D. J., Ramsbottom C. A., Storey P. J., 2023, A&A, 678, A170
Bucciantini N., Quataert E., Arons J., Metzger B. D., Thompson T. A., 2008, MNRAS, 383, 25
Burbidge E. M., Burbidge G. R., Fowler W. A., Hoyle F., 1957, Rev. Mod. Phys., 29, 547
Cameron A. G. W., 1957, Pub. Astron. Soc. Pac., 69, 201
Cartier R. et al., 2024, preprint(arxiv:2410.21381)
Clocchiatti A., Suntzeff N. B., Covarrubias R., Candia P., 2011, AJ, 141, 163
Cowan J. J., Sneden C., Lawler J. E., Aprahamian A., Wiescher M., Langanke K., Martínez-Pinedo G., Thielemann F.-K., 2021, Rev. Mod. Phys., 93, 15002
Côté B. et al., 2019, ApJ, 875, 106
Davey A. R., Storey P. J., Kisielius R., 2000, A&AS, 142, 85
Dean C., Fernández R., 2024, Phys. Rev. D, 110, 083024
Dere K. P., Landi E., Mason H. E., Fossi B. C. M., Young P. R., 1997, A&AS, 125, 149
Dessart L., Livne E., Waldman R., 2010, MNRAS, 405, 2113
Dessart L., Hillier D. J., Livne E., Yoon S.-C., Woosley S., Waldman R., Langer N., 2011, MNRAS, 414, 2985
Dessart L., Hillier D. J., Yoon S.-C., Waldman R., Livne E., 2017, A&A, 603, A51
Domoto N., Tanaka M., Wanajo S., Kawaguchi K., 2021, ApJ, 913, 26
Domoto N., Tanaka M., Kato D., Kawaguchi K., Hotokezaka K., Wanajo S., 2022, ApJ, 939, 8
Eichler D., Livio M., Piran T., Schramm D. N., 1989, Nature, 340, 126
Filippenko A. V. et al., 1995, ApJ, 450, L11
Freiburghaus C., Rosswog S., Thielemann F.-K., 1999, ApJ, 525, L121
Fujibayashi S., Sekiguchi Y., Shibata M., Wanajo S., 2023, ApJ, 956, 100
Galama T. J. et al., 1998, Nature, 395, 670
Galavís M. E., Mendoza C., Zeippen C. J., 1998, A&AS, 133, 245
Georgy C., Meynet G., Walder R., Folini D., Maeder A., 2009, A&A, 502, 611
Gillanders J. H., Smartt S. J., Sim S. A., Bauswein A., Goriely S., 2022, MNRAS, 515, 631
Guttman O., Shenhar B., Sarkar A., Waxman E., 2024, MNRAS, 533, 994
Hamuy M. et al., 2002, AJ, 124, 417
Hillier D. J., Dessart L., 2012, MNRAS, 424, 252
Horowitz C. J. et al., 2019, J. Phys. G: Nucl. Part. Phys., 46, 083001
Hotokezaka K., Nakar E., 2020, ApJ, 891, 152
Hotokezaka K., Piran T., Paul M., 2015, Nat. Phys., 11, 1042
Hotokezaka K., Beniamini P., Piran T., 2018, Int. J. Mod. Phys., D27, 1842005
Hotokezaka K., Tanaka M., Kato D., Gaigalas G., 2021, MNRAS, 506, 5863
Hotokezaka K., Tanaka M., Kato D., Gaigalas G., 2022, MNRAS, 515, L89
Hotokezaka K., Tanaka M., Kato D., Gaigalas G., 2023, MNRAS, 526, L155
Hunter D. J. et al., 2009, A&A, 508, 371
Iwamoto K. et al., 1998, Nature, 395, 672
Ji A. P., Frebel A., Chiti A., Simon J. D., 2016, Nature, 531, 610
Just O., Aloy M. A., Obergaulinger M., Nagataki S., 2022, ApJ, 934, L30
Kamiński T., Mason E., Tylenda R., Schmidt M. R., 2015, A&A, 580, A34
Kirby E. N., Duggan G., Ramirez-Ruiz E., Macias P., 2020, ApJ, 891, L13
Kobayashi C. et al., 2023, ApJ, 943, L12
Kohri K., Narayan R., Piran T., 2005, ApJ, 629, 341
Kramida A., Yu. Ralchenko Reader J., and NIST ASD Team, 2021, NIST Atomic Spectra Database (ver. 5.9), [Online]. Available: https://physics.nist.gov/asd [2017, April 9]. National Institute of Standards and Technology, Gaithersburg, MD.
Lattimer J. M., Schramm D. N., 1974, ApJ, 192, L145
Levan A. J. et al., 2023, Nature, 626, 737
Li L.-X., Paczynski B., 1998, ApJ, 507, L59
Liu Y.-Q., Modjaz M., Bianco F. B., Graur O., 2016, ApJ, 827, 90
Livne E., 1993, ApJ, 412, 634
MacFadyen A. I., Woosley S. E., 1999, ApJ, 524, 262
Macias P., Ramirez-Ruiz E., 2018, ApJ, 860, 89
Madonna S. et al., 2018, ApJ, 861, L8
Maeda K., Mazzali P. A., Deng J., Nomoto K., Yoshii Y., Tomita H., Kobayashi Y., 2003, ApJ, 593, 931
Mao J., Badnell N. R., Del Zanna G., 2020, A&A, 643, A95
Maoz D., Nakar E., 2025, ApJ, 982, 179
Mazzali P. A. et al., 2006, Nature, 442, 1018
Meléndez M., Bautista M. A., Badnell N. R., 2007, A&A, 469, 1203
Merle T., Thévenin F., Zatsarinny O., 2015, A&A, 577, A113
Metzger B. D., 2020, Living Rev. Relativ., 23, 1
Metzger B. et al., 2010, MNRAS, 406, 2650
Metzger B. D., Giannios D., Thompson T. A., Bucciantini N., Quataert E., 2011, MNRAS, 413, 2031
Miller J. M., Sprouse T. M., Fryer C. L., Ryan B. R., Dolence J. C., Mumpower M. R., Surman R., 2020, ApJ, 902, 66
Modjaz M., Liu Y. Q., Bianco F. B., Graur O., 2016, ApJ, 832, 108
Molero M., Simonetti P., Matteucci F., della Valle M., 2020, MNRAS, 500, 1071
Mösta P., Roberts L. F., Halevi G., Ott C. D., Lippuner J., Haas R., Schnetter E., 2018, ApJ, 864, 171
Mulholland L. P., McElroy N. E., McNeill F. L., Sim S. A., Ballance C. P., Ramsbottom C. A., 2024a, MNRAS, 532, 2289
Mulholland L. P., McNeill F., Sim S. A., Ballance C. P., Ramsbottom C. A., 2024b, MNRAS, 534, 3423
Nahar S. N., 1995a, ApJS, 101, 423
Nahar S. N., 1995b, A&A, 293, 967
Nahar S. N., 1996, Phys. Rev. A, 53, 2417

Nahar S. N., 1997, Phys. Rev. A, 55, 1980
Nahar S. N., 1999, ApJS, 120, 131
Nahar S. N., Bautista M. A., 2001, ApJS, 137, 201
Nahar S. N., Pradhan A. K., 1996, A&AS, 119, 509
Nahar S. N., Bautista M. A., Pradhan A. K., 1997, ApJ, 479, 497
Nakamura T., Mazzali P. A., Nomoto K., Iwamoto K., 2001, ApJ, 550, 991
Nishimura S., Kotake K., Hashimoto M.-a., Yamada S., Nishimura N., Fujimoto S., Sato K., 2006, ApJ, 642, 410
Nomoto K. et al., 2000, AIP Conf. Proc., 526, 622
Nussbaumer H., Storey P. J., 1986, A&AS, 64, 545
Pasternack S., 1940, ApJ, 92, 129
Patat F. et al., 2001, ApJ, 555, 900
Paxton B., Bildsten L., Dotter A., Herwig F., Lesaffre P., Timmes F., 2011, ApJS, 192, 3
Paxton B. et al., 2015, ApJS, 220, 15
Pelan J., Berrington K. A., 1995, A&AS, 110, 209
Pelan J., Berrington K. A., 1997, A&AS, 122, 177
Perego A., Thielemann F. K., Cescutti G., 2021, in Bambi C., Katsanevas S., Kokkotas K.D., eds, Handbook of Gravitational Wave Astronomy. Springer, Singapore, p. 1
Perego A. et al., 2022, ApJ, 925, 22
Pognan Q., Jerkstrand A., Grumer J., 2022a, MNRAS, 510, 3806
Pognan Q., Jerkstrand A., Grumer J., 2022b, MNRAS, 513, 5174
Pognan Q., Grumer J., Jerkstrand A., Wanajo S., 2023, MNRAS, 526, 5220
Pognan Q., Wu M.-R., Martínez-Pinedo G., da Silva R. F., Jerkstrand A., Grumer J., Flörs A., 2024, MNRAS, 536, 2973
Prantzos N., Abia C., Cristallo S., Limongi M., Chieffi A., 2020, MNRAS, 491, 1832
Pruet J., Woosley S. E., Hoffman R. D., 2003, ApJ, 586, 1254
Rastinejad J. C. et al., 2022, Nature, 612, 223
Rauscher T., Heger A., Hoffman R. D., Woosley S. E., 2002, ApJ, 576, 323
Reichert M. et al., 2023, ApJS, 268, 66
Rodríguez Ó., Nakar E., Maoz D., 2024, Nature, 628, 733
Scofield J. H., 1973, Technical Report UCRL-51326, Theoretical Photoionization Cross Sections from 1 to 1500 keV. California Univ., Lawrence Livermore Lab., Livermore, CA, US
Shankar S., Mösta P., Barnes J., Duffell P. C., Kasen D., 2021, MNRAS, 508, 5390
Sharon A., Kushnir D., 2020, MNRAS, 496, 4517
Shortley G. H., 1940, Phys. Rev., 57, 225
Siegel D. M., Barnes J., Metzger B. D., 2019, Nature, 569, 241
Siegel D. M., Agarwal A., Barnes J., Metzger B. D., Renzo M., Villar V. A., 2022, ApJ, 941, 100
Sigut T. A. A., Pradhan A. K., 1995, J. Phys. B At. Mol. Phys., 28, 4879
Sneppen A., Watson D., 2023, A&A, 675, A194
Sneppen A., Watson D., Damgaard R., Heintz K. E., Vieira N., Väisänen P., Mahoro A., 2024a, A&A, 690, A398
Sneppen A., Damgaard R., Watson D., Collins C. E., Shingles L., Sim S. A., 2024b, A&A, 692, A134
Sollerman J., Kozma C., Fransson C., Leibundgut B., Lundqvist P., Ryde F., Woudt P., 2000, ApJ, 537, 127
Storey P. J., 1994, A&A, 282, 999
Storey P. J., Sochi T., 2016, MNRAS, 459, 2558
Storey P. J., Zeippen C. J., Sochi T., 2016, MNRAS, 456, 1974
Stritzinger M. D. et al., 2024, A&AS, 686, A79
Surman R., McLaughlin G. C., Hix W. R., 2006, ApJ, 643, 1057
Symbalisty E. M. D., Schramm D. N., Wilson J. R., 1985, ApJ, 291, L11
Tanaka M., Hotokezaka K., 2013, ApJ, 775, 113
Tanaka M. et al., 2023, ApJ, 953, 17
Tarumi Y., Hotokezaka K., Domoto N., Tanaka M., 2023, preprint(arxiv:2302.13061)
Tayal S. S., Henry R. J. W., 1996, J. Phys. B Atom. Mol. Phys., 29, 3443
van Regemorter H., 1962, ApJ, 136, 906
Wallner A. et al., 2015, Nat. Commun., 6, 5956
Wang J. et al., 2018, ApJ, 867, 147
Watson D. et al., 2019, Nature, 574, 497
Wheeler J. C., Yi I., Höflich P., Wang L., 2000, ApJ, 537, 810
Winteler C., Kaeppeli R., Perego A., Arcones A., Vasset N., Nishimura N., Liebendoerfer M., Thielemann F.-K., 2012, ApJ, 750, L22
Woosley S. E., 1993, ApJ, 405, 273
Woosley S. E., Eastman R. G., Schmidt B. P., 1999, ApJ, 516, 788
Zanna G. D., Dere K. P., Young P. R., Landi E., 2021, ApJ, 909, 38
Zhang H., 1996, A&AS, 119, 523
Zhang H. L., Pradhan A. K., 1995, A&A, 293, 953
Zhang H. L., Pradhan A. K., 1997, A&AS, 126, 373

APPENDIX A: DATA FOR ENERGY LEVELS, RADIATIVE TRANSITION RATES, AND COLLISION STRENGTHS OF ELEMENTS WITH $Z \leq 28$

Energy levels are taken from the NIST ASD (Kramida et al. 2021).

(i) For iron group elements ($Z = 26, 27, 28$), the radiative transition rates are taken from the NIST data base for Fe I, IV, Co I, Ni I, II, III, and IV, while from Nahar (1995b) for Fe II, Nahar & Pradhan (1996) for Fe III, Storey, Zeippen & Sochi (2016) for Co II, and Storey & Sochi (2016) for Co III. For Co I and IV, we calculate M1 transition rates using the analytic formula based on LS coupling (Pasternack 1940; Shortley 1940; Bahcall & Wolf 1968):

$$A_{ul} = 1.3\,\mathrm{s}^{-1} \left(\frac{\lambda_{ul}}{4\,\mu\mathrm{m}}\right)^{-3} f(J_u, L_u, S_u)\,, \tag{A1}$$

where λ_{ul} is the line wavelength for the transition between the upper level u and lower level l, and $f(J, L, S)$ is an algebraic factor, i.e.

$$f(J, L, S) = \frac{(J^2 - (L-S)^2)((L+S+1)^2 - J^2)}{12J(2J+1)} \tag{A2}$$

for $J_u = J_l + 1$, and

$$f(J, L, S) = \frac{((J+1)^2 - (L-S)^2)((L+S+1)^2 - (J+1)^2)}{12(J+1)(2J+1)} \tag{A3}$$

for $J_u = J_l - 1$, where J is the total angular momentum, L the total orbital angular momentum, and S the total spin angular momentum, in units of $\hbar$. Collision strength data are taken from Pelan & Berrington (1997) for Fe I, Zhang & Pradhan (1995) for Fe II, Zhang (1996) for Fe III, Zhang & Pradhan (1997) for Fe IV, Storey et al. (2016) for Co II, Storey & Sochi (2016) for Co III, and Bautista (2004) for Ni II. The collision strengths for the lowest levels of the ground configuration of Ni III are taken from Blondin et al. (2023). We use the collision strengths of Co III for Ni IV. For the missing iron group collision data, we use the formula from van Regemorter (1962) for E1 transitions, and the constant value $\Omega_F = 0.5$ for forbidden transitions.

(ii) For light elements ($Z \leq 25$), we take from the NIST data base the radiative transition rates for C I, II, N I, II, III, O I, II, III, IV, F I, II, III, IV, Ne II, III, Na I, III, IV, Mg I, II, IV, Al I, II, Si I, II, P I, II, III, S I, II, III, IV, Cl I, II, III, IV, Ar II, III, IV, K I, III, IV, Ca I, II, IV, Sc I, II, Ti I, II, VI, II, IV, Cr II, IV, and Mn I. We use equation (A1) to obtain M1 transitions for C III, IV, N IV, Ne IV, Al III, IV, Si III, IV, P IV, Sc III, IV, Ti III, IV, VIII, Cr I, III, Mn II, III, and IV. We use the collision strengths given by (Bhatia & Kastner 1995) for O I, (Mao, Badnell & Del Zanna 2020) for O II, (Storey et al. 2016) for O III, (Merle, Thévenin & Zatsarinny 2015) for Mg I, (Sigut & Pradhan 1995) for Mg II, (Tayal & Henry 1996) for Ar II, (Galavís, Mendoza & Zeippen 1998) for Ar III, (Meléndez, Bautista & Badnell 2007) for Ca II, and (Pelan & Berrington 1995) for Ca IV. The remaining collision data for light elements are again computed with the van Regemorter (1962) formula, and $\Omega_F = 0.5$.

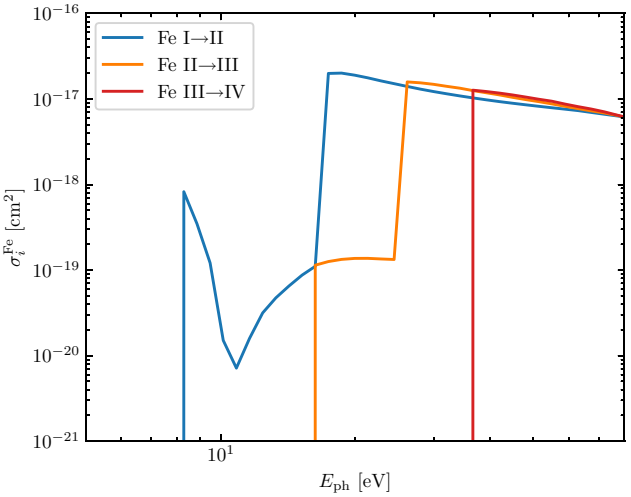

Figure B1. Photoionization cross-section as a function of the photon energy for Fe ions, computed using HULLAC without resolving the fine structure levels.

APPENDIX B: IMPACT OF PHOTOIONIZATION FROM RECOMBINATION PHOTONS

We report in Fig. B1 the photoionization cross-sections computed using HULLAC in the non-relativistic configuration mode for the first Fe ions. The cross-sections peak just above the ionization threshold of the ions, with a power-law decrease at higher energies. These calculations serve as basis for our estimate of the photoionization rate from recombination photons $\gamma_{\rm rec}$. We test the relevance of such contribution to ionization by considering the model parameter space explored in Section 4. Fig. B2 shows the ratio between such contribution and that provided by non-thermal β-particles coming from radioactive decays $\gamma_{\rm rad}$, for all the atomic species in the considered mixture. The results are displayed for the equal-mass Fe–Nd case, but they qualitatively hold also for the pure Fe and pure Nd cases, and by extension for other generic compositions. The importance of this ionization mechanism heavily depends on the ionization stage of the targeted atomic species, while it is less dependent on the element itself. For a high stage of ionization, such as III → IV, photoionization is absent, since only higher energy photons with a few tens eV can ionize the target ions. On the contrary, most of the recombination photons lie in an energy range one order of magnitude lower. As a result, the higher impact is observed for the ionization of stage I → II, while the stage II → III is only partially impacted, mostly by photons from the recombination of stage IV → III. This effect has thus a clear dependence on the kinetic temperature, whereas such higher stages are most likely to be found at higher $T_{\rm e}$ (see also Figs 1 and 2). As a result, for most of the explored parameter space, the ionization of neutral Fe is driven in comparable measure by the two modelled sources of ionization. At lower densities and higher values of input heating, the contribution from recombination photons can even surpass the

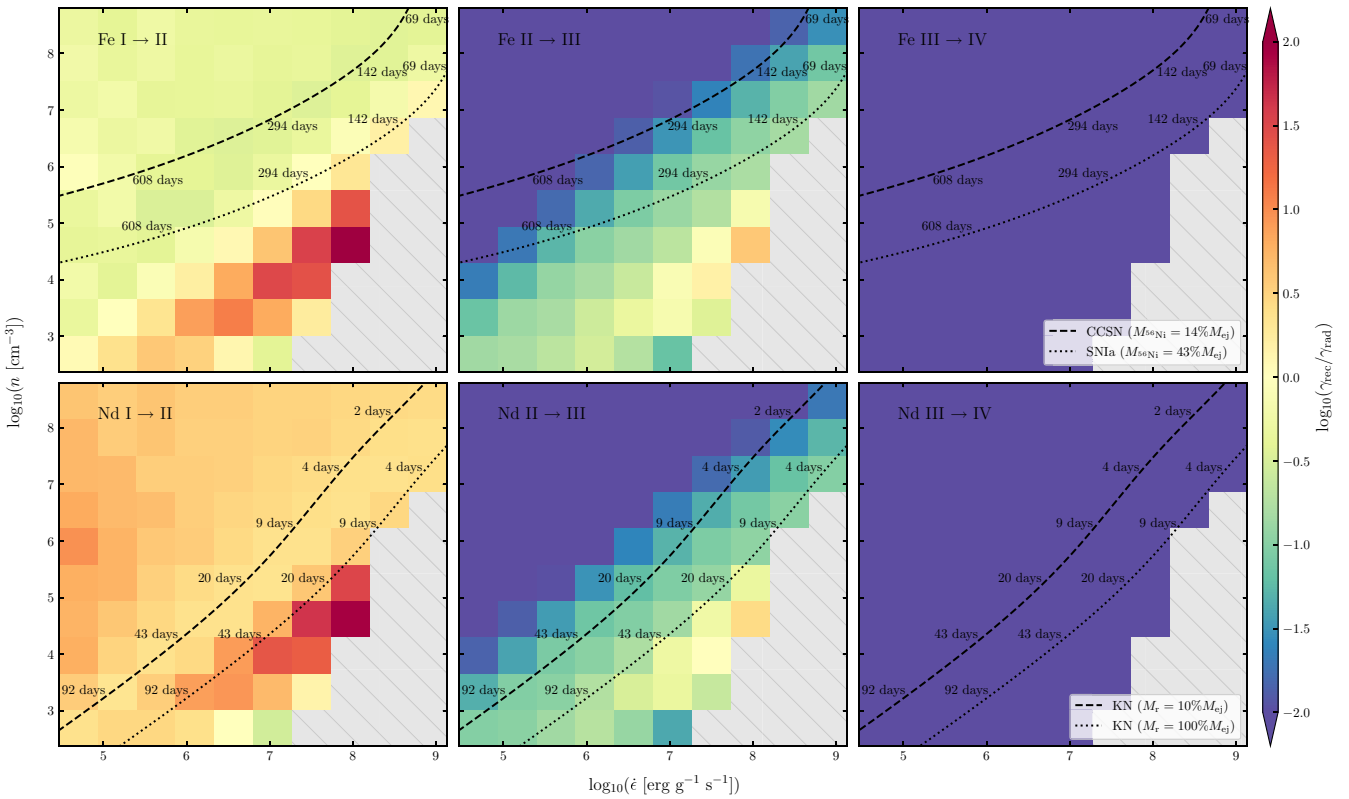

Figure B2. Ratio between the contribution to the ionization rate per atom coming from recombination photons and the contribution coming from decay β-particles, as a function of the specific energy deposition rate and the number density of atoms. The rates are computed for a mixture of 50 per cent Fe I–IV and 50 per cent Nd I–IV in mass fraction, on a 10 × 10 grid log-spaced, using ionization and thermal balance. Each panel shows a different ionizing species. For approximate visual reference, we superimpose to Fe rates (upper panels) plausible trajectories with their time evolution of a CC SN and a SN Ia, while we consider a KN with two degrees of r-process material dilution for Nd rates (lower panels).

one from radioactivity by one order of magnitude or more. This effect is even more relevant for the neutral Nd case, in which the photoionization dominates for the entirety of the parameter space. In this regard, however, we note that these estimates are obtained by employing a certain number of assumptions on the photoionization cross-sections of the different ions, and by constructing a very rough recombination photon spectrum. Therefore, despite the generality of the qualitative trends, we expect potential quantitative changes in the magnitude of the photoionization impact, once better treatments for this process are included.

APPENDIX C: CONVERGENCE OF THE EJECTA ZONE MODEL

We show in Fig. C1 the effect of varying the number of zones used to describe the ejecta on the predicted optical to near-IR spectrum of SN 1998bw. Starting from the three zones adopted in Section 7, we show a two-zone model derived by merging the two outermost shells, and a single-zone model obtained by averaging all the relevant quantities on the entire outflow. In parallel, we report a four-zone model, constructed by splitting in two zones of roughly equal mass the innermost shell. The latter is the only ejecta region still featuring some variability in the compositional profiles of the r0e2 ejecta model from Dessart et al. (2017), which is averaged out in the three-zone model. As visible in Fig. C1, the convergence of the spectrum is rather rapid, both in terms of overall flux distribution and of individual important lines that dominate the cooling. The single-zone model is already not overly far from the higher resolution models, with the major difference being the lower intensity of the Ca II 7300 Å doublet and the higher intensity of the C I 8730 Å triplet. The relevant Ca II line reaches its final state already when distinguishing between two zones, as it is formed exclusively in the inner one. The C I feature instead weakens as we resolve further the ejecta profile, but it is stable moving from three to four zones. Regardless, as mentioned in Section 7.1, the spectrum in the vicinity of such feature is likely not well reproduced due to the absent modeling of absorptions, and thus the convergence of its shape is less interesting. Finally, we note that in the exploration of the spectrum convergence we do not take into account the Mg I line at 4571 Å, since we model Mg manually within our fiducial three-zone scheme.

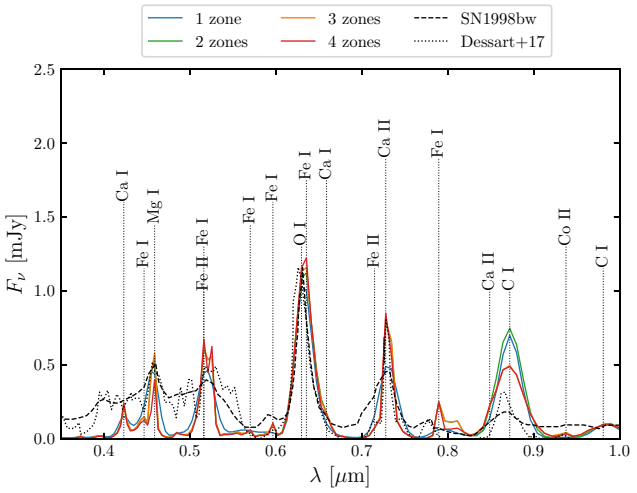

Figure C1. Optical to near-IR spectra targeted on SN 1998bw at 215.4 d post-explosion, modelled using an increasing number of zones in order to describe the r0e2 ejecta model from Dessart et al. (2017). The synthetic spectra from that work, together with the observed SN 1998bw spectra, corrected for redshift and extinction, are shown as reference (dotted and dashed line, respectively).

This paper has been typeset from a TEX/LATEX file prepared by the author.